FINAL TECHNICAL REPORT

October 1, 2003 to September 30, 2007

Award Number DE-FC26-03NT41964

Design, Synthesis, and Mechanistic Evaluation of Iron-Based Catalysis for Synthesis Gas Conversion to Fuels and Chemicals

Principal Investigator Enrique Iglesia
Laboratory for the Science and Application of Catalysis
Department of Chemical Engineering
University of California at Berkeley
Berkeley, CA 94720

Project Personnel Akio Ishikawa (UC-Berkeley)
Manuel Ojeda (UC-Berkeley)
Nan Yao (UC-Berkeley)

DISCLAIMER:

EXECUTIVE SUMMARY

A detailed study of the catalyst composition, preparation and activation protocol of Fe-based catalysts for the Fischer-Tropsch Synthesis (FTS) have been carried out in this project. We have studied the effects of different promoters on the catalytic performance of Fe-based catalysts. Specifically, we have focused on how their sequence of addition dramatically influences the performance of these materials in the Fischer-Tropsch synthesis. The resulting procedures have been optimized to improve further upon the already unprecedented rates and C_{5+} selectivities of the Fe-based catalysts that we have developed as part of this project. Selectivity to C_{5+} hydrocarbon was close to 90 % (CO_2-free basis) and CO conversion rate was about 6.7 mol h^{-1} g-at Fe^{-1} at 2.14 MPa, 508 K and with substoichiometric synthesis gas; these rates were larger than any reported previously for Fe-based FTS catalysts at these conditions. We also tested the stability of Fe-based catalysts during FTS reaction (10 days); as a result, the high hydrocarbon formation rates were maintained during 10 days, though the gradual deactivation was observed. Our investigation has also focused on the evaluation of Fe-based catalysts with hydrogen-poor synthesis gas streams (H_2/CO=1). We have observed that the Fe-based catalysts prepared in this project display also a high hydrocarbon synthesis rate with substoichiometric synthesis gas (H_2/CO=1) stream, which is a less desirable reactant mixture than stoichiometric synthesis gas (H_2/CO=2). We have improved the catalyst preparation protocols and achieved the highest FTS reaction rates and selectivities so far reported at the low temperatures required for selectivity and stability. Also, we have characterized the catalyst structural change and active phases formed, and their catalytic behavior during the activation process to evaluate their influences on FTS reaction. The efforts of this project led to (i) structural evolution of Fe-Zn oxide promoted with K and Cu, and (ii) evaluation of hydrocarbon and CH_4 formation rates during activation procedures at various temperature and H_2/CO ratios. On the basis of the obtained results, we suggest that lower reactor temperature can be sufficient to activate catalysts and lead to the high FTS performance.

In this project, we have also carried out a detailed kinetic and mechanistic study of the Fischer-Tropsch Synthesis with Fe-based catalysts. We have proposed a reaction mechanism with two CO activation pathways: unassisted and H-assisted. Both routes lead to the formation of the same surface monomers (CH_2). However, the oxygen removal mechanism is different. In the H-assisted route, oxygen is removed exclusively as water, while oxygen is rejected as carbon dioxide in the unassisted CO dissociation. The validity of the mechanism here proposed has been found to be in agreement with the experimental observation and with theoretical calculations over a Fe(110) surface. Also, we have studied the validity of the mechanism that we propose by analyzing the H_2/D_2 kinetic isotope effect (r_H/r_D) over a conventional iron-based Fischer-Tropsch catalyst Fe-Zn-K-Cu. We have observed experimentally that the use of D_2 instead of H_2 leads to higher hydrocarbons formation rates (inverse kinetic isotopic effect). On the contrary, primary carbon dioxide formation is not influenced. These experimental observations can be explained by two CO activation pathways.

We have also explored the catalytic performance of Co-based catalysts prepared by using inverse micelles techniques. We have studied several methods in order to terminate the silanol groups on SiO_2 support including impregnation, urea homogeneous deposition-precipitation, or zirconium (IV) ethoxide titration. Although hydroxyl groups on the SiO_2 surface are difficult to be stochiometrically titrated by ZrO_2, a requirement to prevent the formation of strongly-interacting Co oxide species on SiO_2, modification of ZrO_2 on SiO_2 surface can improve the Co clusters dispersion leading to a marked increase in the number of accessible Co sites. Inverse micelle method allowed the synthesis of small Co clusters on SiO_2, but the required surfactant removal steps led to the re-oxidation of Co metal clusters and to the formation of difficult to reduce CoO_x species.

TABLE OF CONTENTS

I. FISCHER-TROPSCH SYNTHESIS ON IRON CATALYSTS

1. Fischer-Tropsch Synthesis on Fe-based with hydrogen-poor synthesis gas.

Over the past 80 years, extensive efforts have been made in the Fischer-Tropsch Synthesis (FTS) field for developing catalysts that maximized conversion of synthesis gas into various types of hydrocarbons. Synthesis gas mixtures can be converted into useful fuels and petrochemicals by using Fe- and Co-based catalysts. An emerging interest in the use of hydrogen-poor synthesis gas (H_2/CO=0.7-1) mixtures as FTS feeds, as a result of the growing use of coal and biomass, led us to consider the use of our previously developed state-of-the-art Fe-based catalysts with such reactant mixtures.

Fe-based catalysts with FTS activities and selectivities similar to those on Co-based catalyst were recently reported by our research group. Those catalysts with unusually high surface areas (~140 m^2 g^{-1}) gave unprecedented activity and C_{5+} selectivity with stoichiometric synthesis gas mixture (H_2/CO=2). These catalysts were prepared by novel synthetic procedures that improve the dispersion and the density of the active structures formed during reaction. Fe-based catalysts generally require the addition of alkali and transition metals in order to improve the FT performance. However, the optimization of catalyst composition with promoter has not been deeply investigated on these Fe-based catalysts with very high surface areas.

We have studied here the FTS performance of Fe-based catalysts promoted with different amounts of K, Cu and Ru. Our investigation was extended in order to evaluate the FTS performance of Fe-based catalysts with hydrogen-poor synthesis gas streams (H_2/CO=1). We have found C_{5+} selectivities close to 90 % (CO_2-free basis) at a CO conversion rate of 6.7 mol h^{-1} g-at Fe^{-1} at 2.14 MPa and 508 K. This rate is larger than any value reported previously in the literature with Fe-based FTS catalysts at these reaction conditions. We have also proved the stability of Fe-based catalysts during FTS reaction (10 days). Towards the end of the project, we briefly examined the viability of Co-based catalysts with high dispersion, prepared via novel deposition techniques and modified supports

1.1. Methodology.

1.1.1. Synthesis of precursors and catalysts.

Fe_2O_3-Zn precursors were prepared by co-precipitation from a mixed solution of Fe and Zn nitrates using ammonium carbonate. Zn was used as a textural promoter that *increased* the surface area of samples during FTS reaction [1]. A solution containing $Fe(NO_3)_3$ (Aldrich, 98 %, 3.0 M) and $Zn(NO_3)_2$ (Aldrich, 98+ %, 1.4 M) at Zn/Fe atomic ratio of 0.1 was added into a large flask containing deionized water (*ca.* 100 cm^3) at 353 K at a rate of 120 cm^3 h^{-1} using a liquid pump. A $(NH_4)_2CO_3$ (Aldrich, 99.9%, 1.0 M) solution was added separately into this flask at rate required to maintain the pH at constant value of 7.0 ± 0.1, measured with a pH meter. The precipitated powders (30 g) were washed five times with isopropanol (*ca.* 30 cm^3 g^{-1} each time). The obtained samples were dried in ambient air at 393 K overnight, and then treated in flowing dry air at 543 K for 4 h; this sample is denoted as the Fe-Zn oxide precursor. The Zn-containing phase formed is $ZnFe_2O_4$ with a cubic fraklinite spinel-type structure [2]. The XRD patterns for the obtained samples, however, showed rhombohedral hematite structure of Fe_2O_3 (with a small amount of α-FeOOH with goethite structure) without detectable $ZnFe_2O_4$ because of the low Zn content.

The Fe-Zn oxide precursors were promoted with K, Cu and/or Ru. Aqueous solutions of K_2CO_3 (Aldrich, 99.99 %), $Cu(NO_3)_2$ (Aldrich, 99.99 %), or ruthenium (III) nitrosylnitrate $[Ru(NO)(NO_3)_x(OH)_y$ (x+y = 3)] (Aldrich, dilute nitric acid solution, Ru 1.5 %) were used as the sources of K, Cu and Ru.

The addition of promoters to Fe-Zn oxide precursors was accomplished using two different

procedures (Scheme 1.1). The first process (route 1) was carried out according to a previously reported study [1]. Potassium was added by incipient wetness impregnation with solutions of the required concentration to give the target K/Fe atomic ratio (K/Fe = 0.06). Next, the solid was dried overnight at 393 K in ambient air. Cu or Ru were then added at a Cu/Fe and Ru/Fe atomic ratio of 0.03 (Cu(Ru)/Fe = 0.03) in a second step, followed by overnight drying at 393 K in ambient air. Finally, the samples were treated in flowing dry air at 543 K for 4 h. The resulting oxide precursors are denoted throughout as Fe-Zn-K_6, Fe-Zn-K_6-Cu_3, and Fe-Zn-K_6-Ru_3, respectively. The subscripts denote the atomic content of the corresponding promoter divided by the Fe atomic content (×100).

The other process (Route 2) was carried out as follows. First, Cu or Ru were added to the Fe-Zn oxide precursor at Cu(Ru)/Fe atomic ratios (Cu(Ru)/Fe = 0.03), followed by overnight drying at 393 K in ambient air and drying at 543 K for 4 h in flowing dry air. Potassium was then added at K/Fe atomic ratios (K/Fe = 0.06) in the second step, followed by overnight drying at 393 K in ambient air. These samples were again treated in flowing dry air at 543 K for 4 h. The resulting oxide precursors are denoted as Fe-Zn-Cu_3-K_6 and Fe-Zn-Ru_3-K_6, respectively. These catalysts were pressed into pellets, lightly crushed, and then sieved to retain the 100-180 μm fraction for FTS reaction.

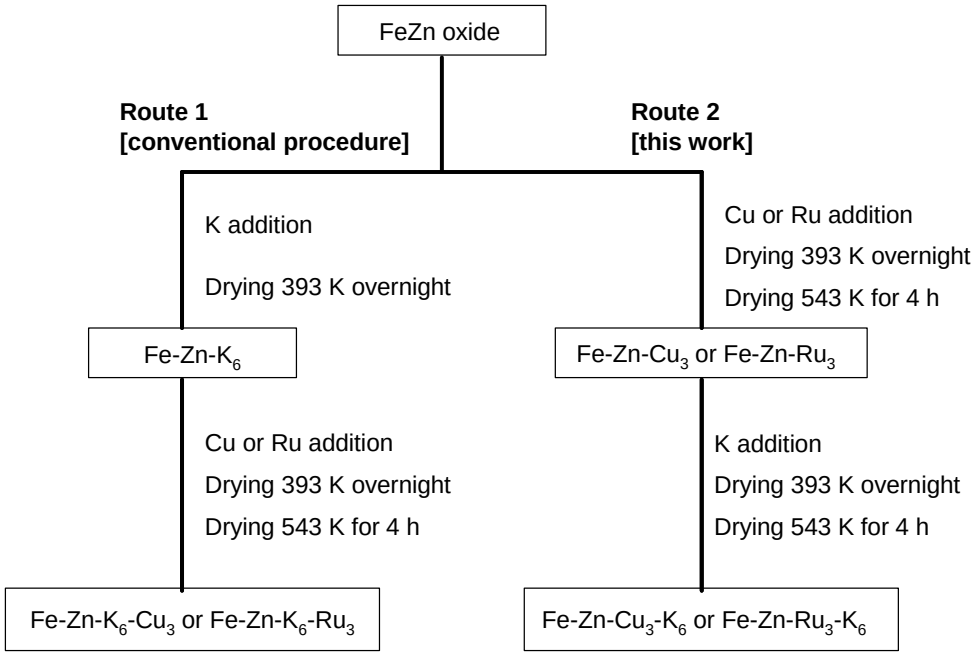

Scheme 1.1. Procedure for preparation of Fe-based catalysts with promoters.

1.1.2. Fischer-Tropsch Synthesis rates and selectivity measurements.

Fischer-Tropsch synthesis rates and selectivities were measured in a single-pass packed-bed reactor with plug-flow hydrodynamics. This reactor was held within a resistively heated three-zone furnace. All lines after the reactor were kept at 433-553 K and a vessel was placed immediately after the reactor and held at 408 K in order to collect liquid products. The reactant and product streams were analyzed on-line using a gas chromatograph (Agilent Technologies, model 6890N). The analysis of N_2, CO, CO_2, and CH_4 was performed using a thermal conductivity detector and a Porapak Q packed-column (15.2 cm × 0.318 cm). All hydrocarbons up to C_{15} were analyzed using a flame ionization detector and a cross-linked methyl silicone capillary column (HP-1, 50 m×0.32 mm; 1.05 μm film).

Fe catalysts (100-180 μm, 0.4 g) were diluted with 11 g of quartz granules (100-180 μm) in

order to avoid temperature gradients. Quartz was washed with concentrated nitric acid and treated in air at 973 K before use. The catalysts were activated using flowing synthesis gas (Praxair; $H_2/CO/N_2$ mixture; 0.62/0.31/0.07, H_2/CO = 2) at 0.1 MPa by increasing the temperature from 298 to 423 K at a rate of 10 K min^{-1} and from 423 to 543 K at 1 K min^{-1}. The catalysts were held at 543 K for 1 h. After the activation process, the temperature was decreased to 508 K, and the synthesis gas (H_2/CO = 2) was switched to a flow of synthesis gas with the target 1:1 H_2:CO ratio (Praxair; $H_2/CO/N_2$ mixture; (0.46/0.46/0.08, H_2/CO = 1). The pressure was then gradually increased to 2.14 MPa. FTS reactions were carried out at 2.14 MPa total pressure and 508 K.

1.2. Effect of promoters on Fischer-Tropsch Synthesis rate and selectivity.

The promotion effects of K, Cu and Ru on the catalytic behavior of Fe-Zn oxide catalysts were examined with sub-stoichiometric synthesis gas reactants (H_2/CO=1) at 508 K and 2.14 MPa. The relative composition of Fe/Zn/K/Cu(or Ru) and BET surface areas are summarized in Table 1.1. Fe-Zn catalysts with various loadings of K, Cu and Ru were obtained by using two different procedures, as described in the experimental section. The measured surface areas were 251-291 m^2 g^{-1} for the oxyhydroxide precipitates obtained by drying in ambient air at 393 K. The heat treatment in flowing air at 543 K for 4 h led to the decrease of the surface area for Fe-Zn oxide because of the sintering of Fe-Zn oxide precursors during the decomposition of the oxyhydroxide precursors. Besides, the addition of K, Cu and/or Ru promoters to Fe-Zn oxides also led to the decrease of their surface areas because of the pore collapse during the evaporation of intrapellet water.

Table 1.2 shows the FTS rates and selectivities obtained with the Fe-based catalysts at similar CO conversion levels. Fe-Zn-K_6 showed the best FT performance (highest C_{5+} selectivity, lowest CH_4 and C_2-C_4 selectivity, especially the olefin contents) compared to those on Fe-Zn-K_4 because K promotes the CO chemisorption and inhibits H_2 chemisorption, which leads to lower FTS rates, higher product molecular weight and greater olefin content [3]. The further increase of K/Fe atomic ratio from 0.06 to 0.08 (Fe-Zn-K_8), however, did not cause significant changes in the FTS performance (data not shown). Therefore, a K/Fe ratio of 0.06 was chosen as optimal to study the effects of Cu and Ru on FTS reaction rates and selectivities. CO conversion rate increased when Ru or Cu was added to Fe-Zn-K_6, suggesting that Ru and Cu species promote carburization and reduction rates. The Ru component is not expected to lead to detectable catalytic contributions at the conditions of these experiments. These promoter effects lead to either a larger number of active sites or to sites with a higher intrinsic activity. In contrast, Fe-Zn-Cu_3-K_6 and Fe-Zn-Ru_3-K_6 prepared by the different promoter introduction protocols, as described in experimental section, showed much higher CO conversion rates and more favorable FTS performance compared to those on Fe-Zn-K_6-Cu_3 and Fe-Zn-K_6-Ru_3. These different FTS performances on Fe-Zn oxides promoted by K and Cu (or Ru) reflect the marked differences in promoter dispersion and placement as a result of the promoter addition protocols.

Table 1.1. List of prepared catalysts and BET surface areas.

	Relative composition (at.%)					BET surface area
	Fe	Zn	K	Cu	Ru	(m^2 g^{-1})
FeZn	100	10	-	-	-	198
$FeZnK_4$	100	10	4	-	-	178

$FeZnK_6$	100	10	6	-	-	168
$FeZnK_6Cu_3$	100	10	6	3	-	141
$FeZnK_6Ru_3$	100	10	6	-	3	147
$FeZnCu_3K_6$	100	10	6	3	-	159
$FeZnRu_3K_6$	100	10	6	-	3	163

Table 1.2. Steady-state performance[a] of Fe-based catalysts (Zn/Fe=0.1) with different loadings of K, Cu, and Ru.

	$FeZnK_4$	$FeZnK_6$	$FeZnK_6Cu_3$	$FeZnCu_3K_6$	$FeZnK_6Ru_3$	$FeZnRu_3K_6$
CO conversion rate (mol h^{-1} g-at Fe^{-1})	2.1	2.2	4.4	6.7	3.2	5.1
HC formation rate (mol h^{-1} g-at Fe^{-1})	1.5	1.6	3.2	5.1	2.2	3.6
CO_2 selectivity (%)	28.1	29.0	28.3	25.9	31.5	30.7
CH_4 selectivity (%)[b]	4.3	3.9	2.8	1.9	4.5	2.7
C_{5+} selectivity (%)[b]	82.3	84.0	85.7	87.6	80.0	85.5
C_2-C_4 (%)[b]	12.2	11.8	11.2	10.0	14.7	11.1
1-C_5H_{10}/*n*-C_5H_{12}	2.3	2.5	2.8	3.1	2.5	2.7
1-$C_{10}H_{20}$/*n*-$C_{10}H_{22}$	0.5	1.5	1.3	2.1	1.5	1.8

[a] $H_2/CO=1$, 508 K, 2.14 MPa, CO conversion = 12-18 %.
[b] CH_4, C_{5+}, and C_2-C_4 selectivities are reported on a CO_2-free basis.

Many studies have described the phenomenological effects of promoters on FTS [4-6], without specific or rigorous attention to the effects of addition sequence. Therefore, we discuss here the differences in FTS performance between Fe-Zn-K_6-$Cu(Ru)_3$ and Fe-Zn-$Cu(Ru)_3$-K_6 from the point view of promoter addition sequence. Aqueous solutions of $Cu(NO_3)_2$ and $Ru(NO)(NO_3)_x(OH)_y$ were used as the source of Cu and Ru promoters. The pH values of the aqueous solutions of Cu and Ru complexes were 3.0 and 0.3, respectively. In the case of Fe-Zn-Cu_3-K_6 and Fe-Zn-Ru_3-K_6 samples with high FTS activity, Cu or Ru precursors were loaded onto Fe-Zn oxide and then the samples were treated at 543 K before K_2CO_3 addition. In contrast, Fe-Zn-K_6-Cu_3 and Fe-Zn-K_6-Ru_3 samples, with lower FTS activity were obtained by the addition of K_2CO_3 followed by impregnation with Cu or Ru precursors. In the latter protocols, the acidic solutions containing Cu and Ru complexes, unstable species in basic media, were added to Fe-Zn oxide and K_2CO_3 particles on the surface of Fe-Zn oxide. The neutralization reaction of acidic species and K_2CO_3 would then result from the addition of metal nitrate solutions, suggesting that these reactions caused the rapid precipitation of $Cu(NO_3)_2$ and $Ru(NO)(NO_3)_x(OH)_y$ complexes to form large hydroxide crystallites, while K_2CO_3 is converted to KNO_3. Consequently, the particles of precipitated Cu and Ru hydroxides on the surface of Fe-Zn oxides would become larger and more heterogeneous on the surface during rapid precipitation compared to those promoted without neutralization. This low dispersion of promoters on the surface would lead to unfavorable FTS performance (higher CH_4, lower C_{5+} selectivity and the decrease of FTS rates) on Fe-Zn-K_6-Cu_3 and Fe-Zn-K_6-Ru_3

samples, because of poor contacting between promoters and the oxide precursors on which they act.

1.3. Effect of H_2/CO ratio on the Fisher-Tropsch synthesis rate and selectivity (H_2/CO=1 *versus* H_2/CO=2).

The Fe-based catalyst promoted with K and Cu (Fe-Zn-Cu_3-K_6) showed the highest CO conversion rates with sub-stoichiometric synthesis gas streams (H_2/CO=1). We compare here the FT performance of prepared iron-based catalyst under stoichiometric synthesis gas (H_2/CO=2) to that in hydrogen-poor reactants (H_2/CO=1). The selectivities and steady-state FTS rates on Fe-Zn-Cu_3-K_6 are shown in Figure 1 as a function of CO conversion, varied by changes in space veloscity. These data were obtained by changing the CO space velocity at constant temperature (508 ± 0.5 K). Stoichiometric synthesis gas led to lower CO_2 selectivities and higher hydrocarbon formation rates, but also to slightly lighter products (higher CH_4, a little lower C_{5+} selectivity; by 2-5%; data not shown) and lower olefin content.

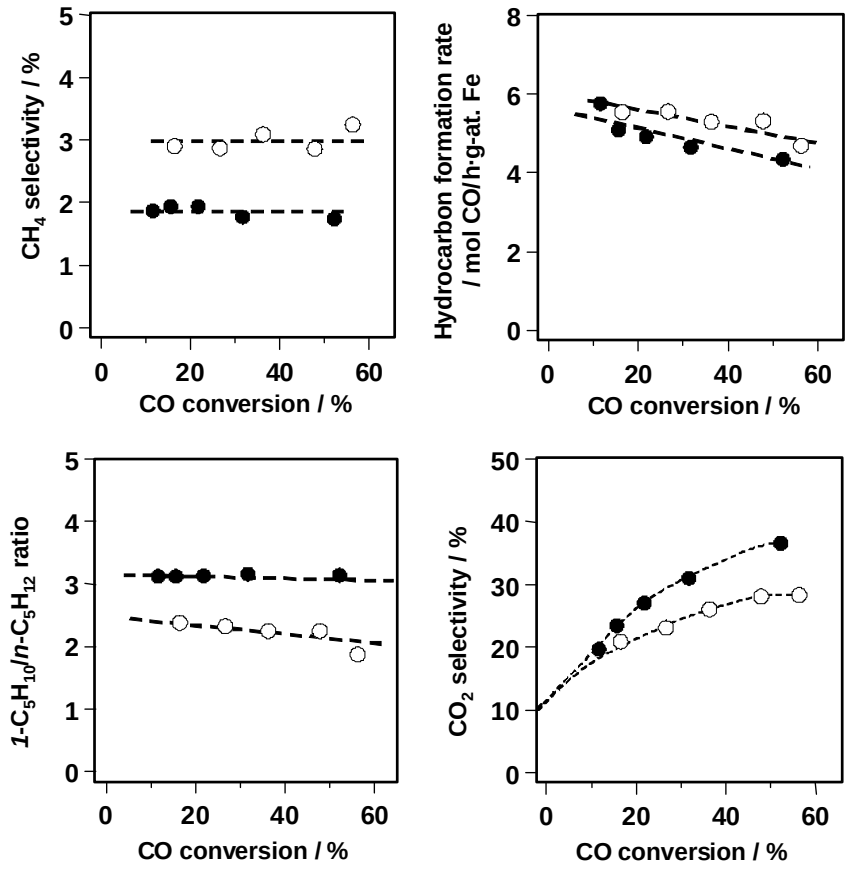

Figure 1.1. Steady state FTS rates and selectivities on Fe-Zn-Cu_3-K_6 catalyst as a function of CO conversion under synthesis gas stream with H_2/CO=1 (closed circles) and H_2/CO=2 (open circles) at 508 K and 2.14 MPa.

Fe-based catalysts are able to reject O-atoms from CO as both H_2O and CO_2. Therefore, H_2O and CO_2 both form as primary FTS products on Fe-based catalysts:

$$2\ H_2 + CO \rightarrow (\text{-}CH_2\text{-})_n + H_2O \quad (1.1)$$
$$H_2 + 2CO \rightarrow (\text{-}CH_2\text{-})_n + CO_2 \quad (1.2)$$

The H_2O formed as a primary product during FTS reactions can react with CO to give CO_2 *via* secondary water-gas shift (WGS) reactions:

$$CO + H_2O \rightarrow CO_2 + H_2 \quad (1.3)$$

O-atom rejection to form H_2O seems to be the favorable pathway under stoichiometric synthesis gas stream [7], while O-atom rejection to form CO_2 would become an important pathway in CO-rich synthesis gas streams. WGS reactions also become an important pathway with increasing H_2O concentration for all synthesis gas stoichiometries. As shown in Figure 1, CO_2 selectivities increased with increasing CO conversion for both sub-stoichiometric and stoichiometric synthesis gas streams. The local slopes of CO_2 selectivities vs. CO conversion (or residence time) reflect the contributions of water-gas shift reactions to CO_2 formation selectivities [7]. Therefore, the larger local slopes of CO_2 selectivities with sub-stoichiometric reactants indicate that low H_2/CO ratio favor secondary WGS rates. In contrast, the extrapolated y-intercepts in Figure 1b are almost same in both cases, suggesting that different H_2/CO ratio led to no significant change in the relative rates of removal of chemisorbed O-atoms using CO to form CO_2. Therefore, the decrease of H_2/CO ratio led to strong contribution of WGS reaction to FTS reaction, suggesting that Fe-Zn-Cu_3-K_6 provides active sites for WGS reaction and allows the efficient use of synthesis gas with sub-stoichiometric H_2/CO ratios by using the majority CO species as the oxygen rejection co-reactant.

1.4 Catalytic stability of Fe-Zn-Cu_3-K_6 materials.

The Fisher-Tropsch synthesis was carried out on optimal Fe-Zn-Cu_3-K_6 catalysts at 508 K and 2.14 MPa under synthesis gas stream (5.0 NL $h^{-1}g_{cat}^{-1}$) with H_2/CO=1 for 240 h in order to examine the stability of this catalyst. Figure 1.2 shows the dependence of CO conversion and hydrocarbon formation rate with time on stream. A more detailed summary of the catalytic performance is shown in Table 3. The total amount of the formed hydrocarbon with 0.4 g Fe-Zn-Cu_3-K_6 catalyst was estimated to be ~16 kg for 240 h. The rates of CO conversion and hydrocarbon formation on Fe-Zn-Cu_3-K_6 decreased rapidly during an initial period (~9 h). During this initial period, the rapid decrease of FTS performance reflects a decrease in surface area as a consequence of the oxide-carbide interconversions.

After this initial period, the deactivation of the catalyst became slower on Fe-Zn-Cu_3-K_6. The hydrocarbon formation rates and FTS performance obtained after the initial deactivation were reported as steady-state rates and FTS performance in previous sections. The hydrocarbon formation rates, CO_2, C_{5+} selectivities and olefin/paraffin ratio decreased gradually during 240 h, while the amount of the light products formed on the catalyst increased gradually with increasing time on stream. Although the catalytic deactivation would be related to the formation of the inactive species such as carbon on the surface, the sequential changes of FTS performance suggest that promoters become increasingly unavailable at active surfaces. It appears that the small amounts of catalyst granules and promoters are removed out of the reactor by the synthesis gas stream. This is supported by the fact that the wax collected after the reactor was dark, suggesting the presence of Fe carbides.

The procedure proposed in the previous section for the addition of promoters can result in Fe-Zn-Cu_3-K_6 and Fe-Zn-Ru_3-K_6 catalysts with a superior FTS catalytic rates compared to Fe-Zn-K_6-Cu_3 and Fe-Zn-K_6-Ru_3 catalysts prepared by conventional procedures. We have found that the Fe-Zn-Cu_3-K_6 catalyst showed the highest FTS performance among all the catalysts studied here.

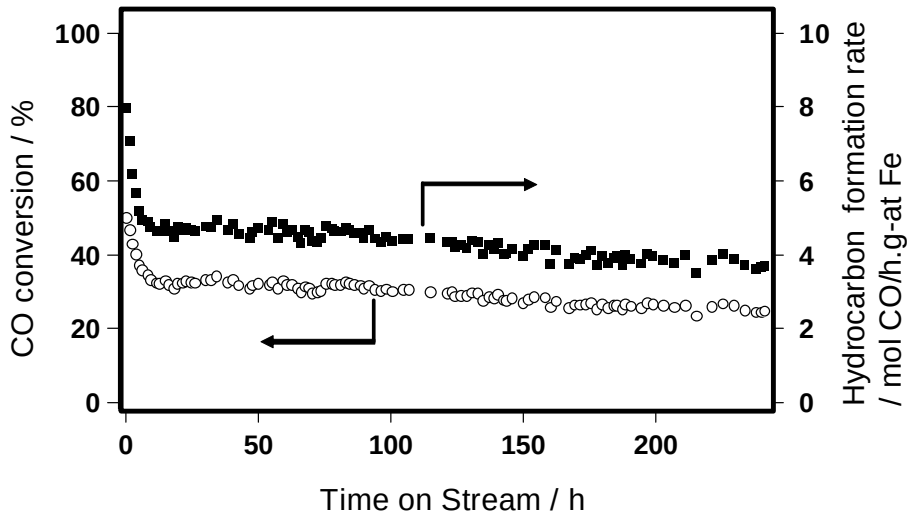

Figure 1.2. CO conversions and hydrocarbon formation rates with time on stream (H_2/CO=1, SV=5.0 NL/h.g-cat.) at 508 K and 2.14 MPa.

Table 1.3. FTS performance in sequence FTS reaction at 508 K and 2.14 MPa with synthesis gas (H_2/CO = 1, SV = 5.0 NL $h^{-1}g_{cat}^{-1}$).

Time on Stream (h)	16	60	86	107	162	185	221	240
CO conversion rate (mol CO/h.g-at.Fe)	6.8	6.8	6.8	6.5	5.9	5.6	5.5	5.2
Hydrocarbon formation rate (mol CO/h.g-at.Fe)	4.6	4.6	4.6	4.4	4.1	4.0	3.9	3.7
CO conversion (%)	31.9	31.9	31.9	30.7	27.6	26.3	26.0	24.6
CO_2 selectivity (%) [a]	31.5	32.0	32.1	32.2	29.7	29.1	30.1	30.0
CH_4 selectivity (%)[a]	2.0	2.2	2.3	2.4	2.4	2.4	2.5	2.5
C_5^+ selectivity (%)	88.6	87.4	86.6	87.1	86.7	86.7	86.1	85.9
1 -C_5H_{10}/*n* -C_5H_{12} ratio	3.1	3.1	3.1	3.0	2.9	2.9	2.9	2.9
1 -$C_{10}H_{20}$/*n* -$C_{10}H_{22}$ ratio	1.6	1.6	1.7	1.5	1.5	1.4	1.5	1.5

[a] CH_4, C_{5+}, and C_2-C_4 selectivities are reported on a CO_2-free basis.

We compare here FTS reaction rates and selectivities on a Fe-Zn-Cu_3-K_6 catalyst with those on previously reported Fe-based catalysts. Fe-Zn-Cu_3-K_6 samples are compared with the most active reported Fe-based catalysts in Table 1.4 at relatively high CO conversions. These Fischer-Tropsch synthesis rates and selectivities were measured in fixed-bed reactor. Low H_2/CO reactant (H_2/CO=1) led to low hydrocarbon productivities relative to those with stoichiometric reactants (H_2/CO = 2). Fe-Zn-Cu_3-K_6 showed the highest hydrocarbon productivity for FTS reaction among all reported catalysts, even though previously reported catalysts were tested at higher temperatures.

Table 1.4. Steady-state FTS performance of various Fe-based catalysts in a fixed-bed reactor.

	$FeZnCu_3K_6$ This work		$FePtK/SiO_2$[a] (8)	Fe/Cu/K[b] (9)
Temperature (K)	508	508	543	533
Pressure (MPa)	2.14	2.14	1.14	1.5
H_2/CO ratio	1.0	2.0	1.0	1.0
GHSV (NL h^{-1} g_{cat}^{-1})	6.8	8.9	1.92	4.0
Syngas conv. (%)	53.4	51.3	53.5	54.8
CO_2 selectivity (%)	36.6	28.1	39.7	45.0
HC productivity (g h^{-1} g_{cat}^{-1})	0.65	0.79	0.1	0.43

[a] $10Fe/1.0Pt/0.2K/88.8SiO_2$
[b] 100Fe/5Cu/4.2K

FTS reaction rates and selectivities on Fe-Zn-Cu_3-K_6 samples in fixed-bed reactors are also compared with FTS performance reported in slurry reactor in Table 1.5 [10-12]. FTS reaction rates and selectivities on Fe-Zn-Cu_3-K_6 samples in fixed-bed reactors were measured at two different conditions, (i) at 508 K, 2.14 MPa, and (ii) at 543 K, 1.31 MPa. Higher temperatures led to higher hydrocarbon productivities even at the lower reactant pressures used. The hydrocarbon synthesis productivity on Fe-Zn-Cu_3-K_6 under synthesis gas stream with H_2/CO=1.0 at 543 K and 1.31 MPa are about 2 times larger than those reported on Fe-$Si_{4.6}$-$K_{1.4}$, even though Fe-Zn-Cu_3-K_6 catalysts were tested under synthesis gas stream with lower H_2/CO ratio (H_2/CO = 1.0 *vs.* 1.7).

Our additional study of synthesis, promotion and activation protocols to increase the density of FTS active site has led to additional improvements in hydrocarbon synthesis productivities. We have reported here the effects of promoters (K, Cu, Ru) on Fisher-Tropsch synthesis rates and selectivities, as well as the effect of two different procedures for promoter addition. The $FeZnCu_3K_6$ catalysts obtained by the efforts carried out as part of this project have led to unprecedented FTS reaction rates and C_{5+} selectivities for hydrogen-poor synthesis gas (H_2/CO = 1) reactants derived from emerging coal and biomass sources.

Table 1.5. Steady-state FTS performance of various Fe-based catalysts using natural gas-derived synthesis gas (H_2/CO = 1.0-1.7).

	$FeZnCu_3K_6$ This work		FeK/SiO_2[a] (10)	$FeCuK/SiO_2$[b] (11)	$FeCuK/SiO_2$[c] (12)
Reactor Type	Fixed-bed		Slurry	Slurry	Slurry
Temperature (K)	508	543	543	533	523
Pressure (MPa)	2.14	1.31	1.31	2.00	1.48
H_2/CO ratio	1.0	1.0	1.7	0.7	0.7
Syngas conv. (%)	53.4	43.3	50.0	67.0	56.1
CO_2 selectivity (%)	36.6	41.1	40.0	–	41.1
HC productivity ($g\ h^{-1}\ g_{cat}^{-1}$)	0.65	1.91	1.00	0.16	0.37

[a] 100Fe/4.6Si/1.4K
[b] 100Fe/5Cu/3K/8SiO_2
[c] 100Fe/4.3Cu/4.1K/25SiO_2

2. Structural evolution and spectroscopic studies of site requirements in Fe catalyzed Fischer-Tropsch synthesis with hydrogen-poor synthesis gas feedstocks.

Iron-based catalysts for the Fischer-Tropsch synthesis form the active sites required by specific catalyst activation processes that are critical to their rate, stability, and selectivity. Several phases of Iron have been found to co-exist during FTS reactions; these include metallic Fe (α-Fe), Fe oxides, and Fe carbides. Fe catalysts are generally activated above reaction temperatures (>500 K) in synthesis gas or CO to form the required active phases.

We have characterized the catalyst structural changes and active phases formed and their catalytic behavior during activation process to evaluate their influence on FTS reactions. The structural change of catalysts and catalytic behavior during activation processes were probed using a combination of X-ray absorption spectroscopy and isothermal transient rates measured from effluent concentrations determined by mass spectrometry and gas chromatography. We report here (i) structural evolution of Fe-Zn oxide promoted with K and Cu, and (ii) hydrocarbon and CH_4 formation rates during activation procedures at various temperature and H_2/CO ratios. On the basis of the obtained results, we suggest that lower reactor temperature can be sufficient to activate catalysts and to maintain high surface areas and site densities and this lead to excellent FTS performance.

2.1. Methodology.

2.1.1. Temperature-programmed reaction and isothermal transient measurements Fischer-Tropsch synthesis rates.

Hydrocarbon, water, and carbon dioxide formation rates during contact with synthesis gas were measured using on-line mass spectrometric analysis. Intensities of 2, 15, 18, 28, 40 and 44 amu were used to measure H_2, CH_4, H_2O, CO, Ar, and CO_2 concentrations, respectively.

Samples (0.2 g) were diluted with quartz granules (2.0 g) and placed within a quartz microreactor. The samples were treated in He (108 mol h^{-1} g-at Fe^{-1}) at 573 K for 1 h, and then cooled to the reaction temperatures before contact with synthesis gas. Temperature-programmed reaction *measurements* were carried out by increasing the temperature from 300 K to 673 K at a rate of 5 K/min in flowing synthesis gas. In isothermal transient experiments, the He stream was switched to a flow of synthesis gas (H_2/CO/Ar, 108 mol h^{-1} g-at Fe^{-1}) at various temperatures. After isothermal transient experiments, the samples were cooled to 508 K and CH_4 formation rates were measured in flowing synthesis gas (H_2/CO/Ar=0.46/0.46/0.08, 108 mol h^{-1} g-at Fe^{-1}) in order to evaluate catalyst performance. BET surface area measurements were carried out after measurements of CH_4 formation rates at 508 K, and He purge (108 mol h^{-1} g-at Fe^{-1}) at 573 K for 1 h, quenching to ambient temperature, and passivation of the samples in flowing 5 vol.% O_2/He at ambient temperature. N_2 physisorption measurements were performed at its normal boiling point (77 K) and surface areas were calculated using the BET method.

2.1.2. X-Ray absorption spectroscopy.

Fe K-edge X-ray absorption spectra were measured for $FeZnCu_3K_6$ during its reduction and carburization in synthesis gas. Fe_2O_3 (Aldrich, %), Fe_3O_4 (Alfa AESAR, 99.997 %), and FeO (Alfa AESAR, 99.5 %), Fe_3C were used as reference crystalline samples. The details of these XAS measurements have been described elsewhere [13]. All X-ray absorption spectra were measured at the Stanford Synchrotron Radiation Laboratory (SSRL). The storage ring was operated at 30-100 mA and 3.0 GeV during the measurements. Two Si(111) crystals detuned by 20 % in order to reject harmonics were used in the monochromator. The spectra were analyzed using WinXAS (version 2.1). Principal component analysis and linear combination methods were used in order to determine the structures present in each sample from spectral features in the near-edge region (6.9-7.4 keV). All samples used in spectroscopic measurements were diluted to 10wt% Fe using graphite powder (Alfa, 99.9995 %), sieved to retain 180-250 μm particles, and placed within an quartz capillary cell. The samples were treated in He (mol h^{-1} g-at Fe^{-1}) at 543 K for 1 h, and then cooled or heated to the reaction temperatures before contacting with synthesis gas.

2.2 Catalytic behavior on iron based catalysts during the activation process.

FTS rates and selectivities for Fe-Zn oxide, Fe-Zn-K_6, and Fe-Zn-Cu_3-K_6 catalysts were measured during isothermal activation processes (543 K) in order to evaluate the relationship between catalyst activation time and FTS performance. These isothermal activation processes were carried out after treating the samples in He (100 cm^3 min^{-1}) at 573 K for 1 h. Figure 2.1 shows the product formation rates on Fe-Zn oxide, Fe-Zn-K_6, and Fe-Zn-Cu_3-K_6 during activation process with hydrogen-poor synthesis gas reactant (H_2/CO=1) at 543 K. Methane and hydrocarbons were immediately formed on Fe-Zn-Cu_3-K_6 after contacting with synthesis gas, and these formation rates reached maximum values after ~1.5 h, respectively. This indicates that the active sites on Fe-Zn-Cu_3-K_6 for FTS reaction were formed immediately after contact with synthesis gas. The formation rates of methane and hydrocarbons over Fe-Zn oxide and Fe-Zn-K_6 increased gradually with time on stream. Several iron phases, such as Fe_3O_4 and Fe_3C, have been postulated in the literature to be the active sites for hydrocarbon formation [14-16]. It seems that the formation of Fe_3O_4 and Fe carbide phases on Fe-Zn oxide and Fe-Zn-K_6 without Cu promoter took place slowly during the initial period (2 h), probably because of the Zn and K components inhibit the reduction of Fe_2O_3 [2]. After 15 h on stream, Fe-Zn oxide showed the highest CH_4 formation rate on Fe-Zn oxide. In contrast, C_{5+} selectivities onr Fe-Zn-K_6 and Fe-Zn-Cu_3-K_6 were 91 and 89%, and much higher than on Fe-Zn oxide (62 %), as a result of the effects of the K promoter.

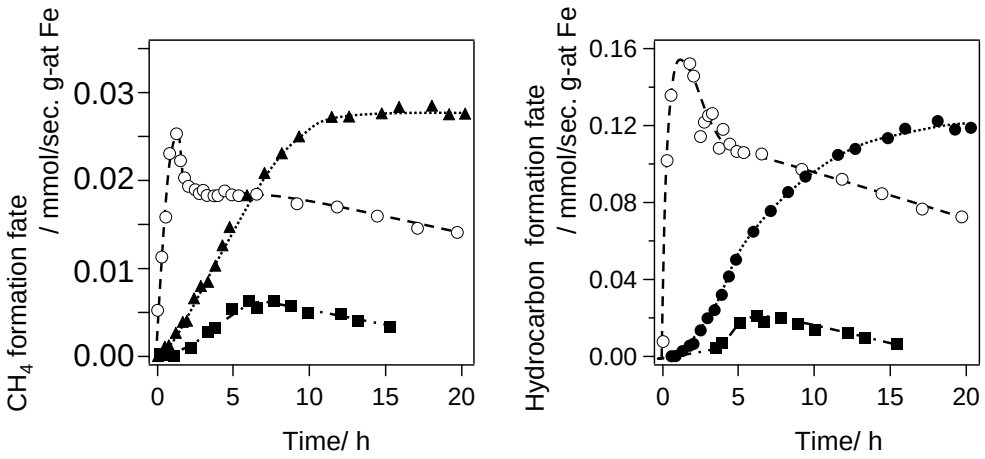

Figure 2.1. CH_4 and hydrocarbon (C_1-C_9) formation rates on iron-based catalysts during activation process. (0.2 g sample; H_2/CO = 1, flow rate: 108 mol/h. g-atom Fe, at 523 K and 0.1 MPa, (○) Fe-Zn-Cu_3-K_6, (■) Fe-Zn-K_6, (▲) Fe-Zn oxide).

After contact with synthesis gas, CH_4 and hydrocarbon formation rates reached maximum values at times that increased in the sequence Fe-Zn-Cu_3-K_6 (1.5 h), Fe-Zn-K_6 (6 h), and Fe-Zn (15 h). Previous studies using mass spectrometry have reported that steady state CH_4 formation rates on both Fe-Zn-K_4 and Fe-Zn-K_4-Cu_2 were attained after 1 h in contact with synthesis gas (H_2/CO = 2) and no detectable change was observed in CH_4 formation rates up to ~8 h [13]. Besides, the CH_4 formation rates were ~10 times higher than the observed rates on Fe-Zn-Cu_3-K_6 in this study, even though both catalysts gave similar FTS performance at 508 K, 2.14 MPa and with stoichiometric synthesis gas (H_2/CO = 2), as described above. The origins of these differences remain unclear at this time and indicate that further investigations of the activation processes for Fe-Zn-Cu_3-K_6 in hydrogen-poor synthesis gas are required to establish the detailed effects of catalyst activation condition on FTS performance.

2.3 Structural evolution studies by X-ray absorption spectroscopy and mass spectrometry.

The structure and nature of iron oxide phases and the reaction products formed during the catalyst activation process were measured by X-ray absorption spectroscopy and mass spectrometry to explore in detail the structure and function of catalysts during activation. FTS rates on Fe-Zn oxide, Fe-Zn-K_6 and Fe-Zn-Cu_3-K_6 (shown in Figure 2.1) indicate that the catalytic activities on the different catalysts cannot be evaluated on the basis of CH_4 formation rates alone because of the different FTS selectivities among these samples. However, the behavior of CH_4 formation rate for a fixed catalyst can be related to its rate of hydrocarbon formation rate. Therefore, the catalytic activities were investigated on the basis of the CH_4 formation rate accurately measured by mass spectrometry here.

2.3.1 In situ structural evolution and products analysis during reactions on Fe-Zn-Cu_3-K_6 in hydrogen-poor synthesis gas.

In situ Fe K-edge X-ray absorption spectroscopy was used to monitor the structural evolution of Fe-Zn-Cu_3-K_6 during activation and FTS reactions. Figure 2.2 shows Fe near-edge spectra for Fe-Zn-Cu_3-K_6 sample during exposure to sub-stoichiometric synthesis gas. Linear combination methods were used to calculate the relative abundance of Fe_2O_3, Fe_3O_4, and FeC_x phases using near-edge spectral features. Figure 2.2 also shows the relative various phases required to describe measured near-edge spectra during reduction and carburization Fe-Zn-Cu_3-K_6 under synthesis gas stream. The formation of Fe_3O_4 was observed above 373 K, and

then the relative abundance of Fe_3O_4 increased, particularly above 450 K. The formation of FeC_x converted from Fe_3O_4 was also observed above 400 K. The relative abundance of Fe_3O_4 decreased above 560 K, and then FeC_x concentration reached 100% at 580 K. The reduction-carburization reaction of the Fe_2O_3 phase stabilized by ZnO requires higher temperature than for pure Fe_2O_3 [2], while Cu decreases the temperature required for reduction-carburization reactions. The reduction and carburization of Fe-Zn-Cu_3-K_6 occurred at ~80 K lower temperatures than that of pure Fe_2O_3 [13].

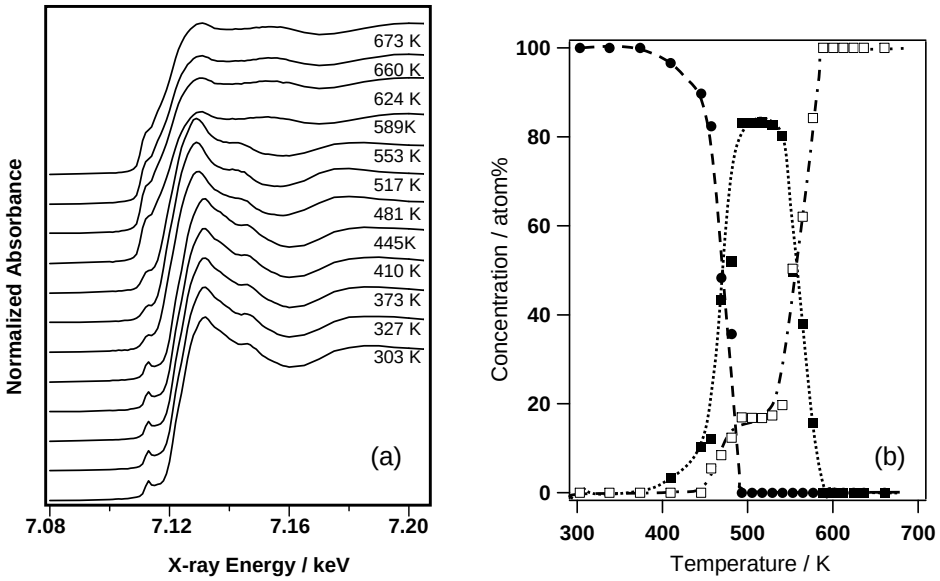

Figure 2.2. In situ Fe K-edge XANES spectra and structural evolution for Fe-Zn-Cu_3-K_6 sample in substoichiometric synthesis gas as a function of temperature. (Fe_2O_3 (●), Fe_3O_4 (■), Fe_xC (□), synthesis gas (H_2/CO=1) flow: 108 mol h^{-1} g-at Fe^{-1}, Fe-Zn-Cu_3-K_6: 1 mg, heating rate: 5 K min^{-1}).

Product formation rates were measured on Fe-Zn-Cu_3-K_6 by transient FTS experiment at the standard reaction conditions (H_2/CO = 1, 543 K, 0.1 MPa) in Figure 2.2. Figure 2.3 shows the products formation rates of CH_4, H_2O and CO_2 during reduction and carburization Fe-Zn-Cu_3-K_6 under synthesis gas stream. The following reactions are observed during transient FTS experiment; (i) the removal of lattice oxygen atoms from Fe_2O_3 and CuO by H_2 to form H_2O or by CO to form CO_2, (ii) the carburization of iron oxide by CO to form CO_2, (iii) FTS reactions of H_2 and CO to form hydrocarbons, H_2O and CO_2, (iv) water-gas shift reactions of CO and H_2O to form CO_2 and H_2. CO_2 formation was observed above near ambient temperature, and then the rate increased with increasing temperature. H_2O formation rate increased above 450 K, while CO_2 formation rate decreased concurrently. CuO is not reduced to Cu metal by CO or H_2 at near ambient temperature [2]. Therefore, the CO_2 formation below ~450 K is assigned to the removal of lattice oxygen atoms by CO from Fe_2O_3 and α-FeOOH, as confirmed by X-ray diffractograms. H_2O formation was observed at temperatures similar to those required for CuO reduction (~470 K) [2]. H_2O is formed both via reduction of CuO and of Fe oxide, the latter catalyzed by the presence of reduced Cu species, which dissociate H_2 required for reduction processes. XAFS results also showed that the Fe_3O_4 formation rates increased above 470 K in Figure 2.1. The formed Cu metal promoted the reduction of Fe_2O_3 to Fe_3O_4 by H_2 corresponding to the literature [2]. Above 540 K, the CO_2 formation rate and the relative abundance of FeC_x formation dramatically increased, and CH_4 formation was also observed concurrently. Therefore, this CO_2 formation occurs via both FTS reactions and via

carburization of iron oxide by CO. CO_2 formation rates above ~620 K reflect FTS and WGS reactions, since FeC_x concentrations have already reached 100 % by these temperatures. CH_4 formation rates increased with increasing amount of active sites and reaction temperature. Therefore, it appears that CH_4 formation rates gradually increased with increasing temperature during this experiment. During transient FTS experiments, temperatures above 540 K were required to form CH_4 on catalyst. In what follows, the catalyst structure and the products formed during catalytic activation process were investigated at temperatures between 508 K (reaction temperature) and 573 K.

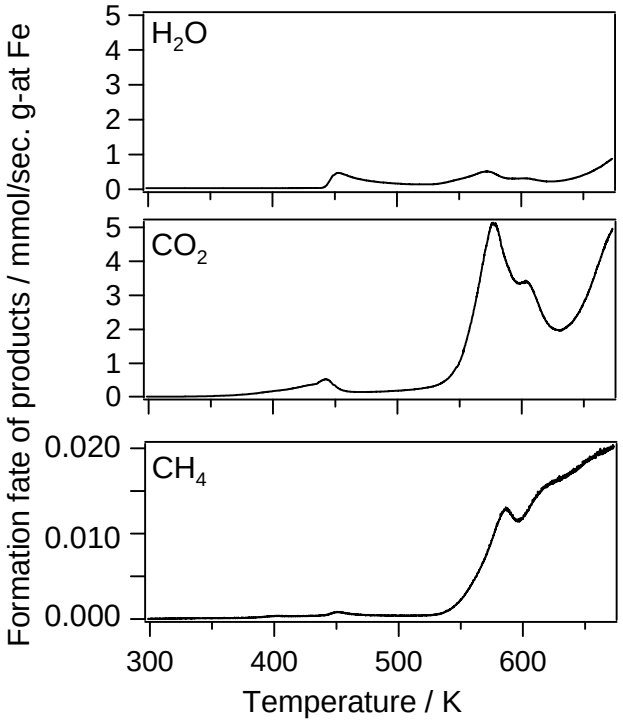

Figure 2.3. Product formation rates as a function of temperature during flow of substoichiometric synthesis gas. (synthesis gas flow: 108 mol h^{-1} g-at Fe^{-1}, Fe-Zn-Cu_3-K_6: 0.2 g, heating rate: 5 K min^{-1}).

2.3.2. In-situ structural characterization and product evolution profiles during catalytic activation at various temperatures.

Figure 2.4 shows formation rates for CH_4, H_2O, and CO_2 on Fe-Zn-Cu_3-K_6 with synthesis gas (H_2/CO = 1) reactants at 543 K and 0.1 MPa as a function of time on stream. Figure 2.4 also shows the concentrations of the Fe_2O_3, Fe_3O_4, and FeC_x phases measured concurrently from near-edge X-ray absorption spectra. During initial contact with synthesis gas (1-2 min), the catalyst temperature increased to ~553 K because of exothermic events, but then stabilized at ~543 K. This initial transient exotherm led to the formation of some Fe metal near the reactor inlet. The previous work has estimated the number of active sites on catalysts after transient FTS experiments by using CO uptake measurement [1,13]. The estimation of the number of active site were, however, too inaccurate because of difficult deconvolution of the complex CO desorption spectra, as a result of the unintended formation of Fe metal near the top of the reactor. As a result, we were unable to estimate the number of active sites on the catalysts by using CO uptake measurements. Instead, we have used CH_4 formation rate measured at 508K, 0.1 MPa, and synthesis gas with H_2/CO of 1 after catalyst activation as a

measure of reactivity and of active site density.

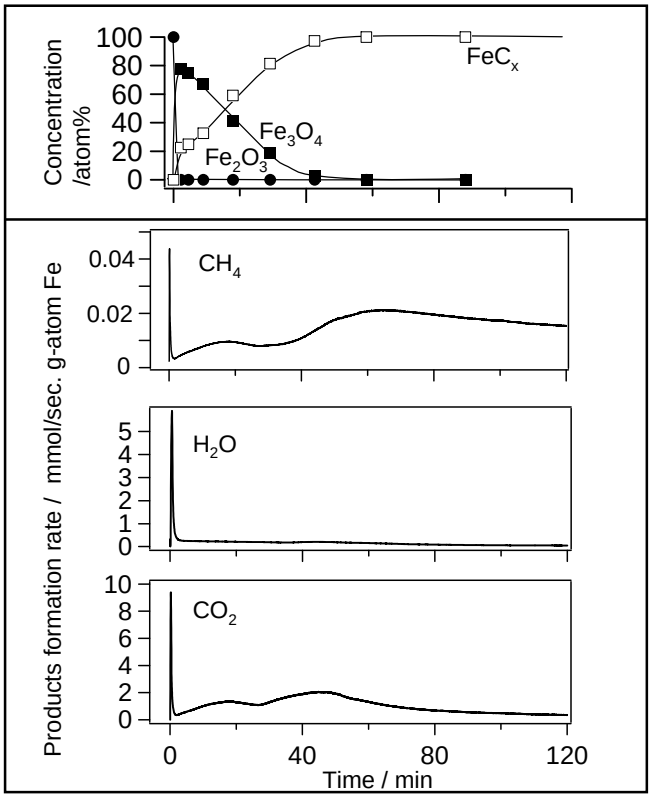

Figure 2.4. Structural evolution measured from X-ray absorption spectra (1 mg sample) and rate of formation of CH_4, H_2O and CO_2 as a function of time on Fe-Zn-Cu_3-K_6 (0.2 g sample) at 543 K. (synthesis gas flow: 108 mol h^{-1} g-at Fe^{-1}).

X-ray absorption spectra for Fe-Zn-Cu_3-K_6 at 543 K changed with time on stream during contact with synthesis gas. Sharp peaks in CH_4, H_2O and CO_2 formation rates were observed after the initial exposure (~1 min) to synthesis gas at 543 K. These sharp peaks were attributed to the reduction of CuO and Fe_2O_3 and the carburization of Fe_3O_4 at near-surface regions of oxide precursors; as a result, the reactor temperature increased up to ~553 K because of the exotermic nature of the carburization of Fe oxides. The removal of lattice oxygen atoms from CuO to form Cu metal occurred during this period because the CuO deposited on catalyst surface is reduced easily to Cu metal at ~540 K. The amount of oxygen removed during this period was, however, larger than the amount of lattice oxygen in CuO. X-ray absorption spectra showed that hematite (Fe_2O_3) disappeared very quickly during initial contact with synthesis gas, while Fe_3O_4 and FeC_x emerged concurrently, consistent with the observed transient exotherm. This latter process is very fast, as indicated by the observation that the concentration of FeC_x reached 20 % after 1 min. Therefore, the initial exposure to synthesis gas at 543 K led to the removal of oxygen from the surface and bulk of Fe_2O_3 to form Fe_3O_4 and then to the introduction of carbon into the Fe structure to form FeC_x. The extent of catalyst carburization increased with the reaction time, until FeC_x became the only detectable crystallographic phase after 45 min.

The sharp peak corresponding to water formation was observed initially, as described above, and then decreased with time on stream. In contrast, CO_2 formation rates showed two broad formation rate peaks. The first CO_2 formation feature reflects the reduction of hematite to form magnetite, while the second peak arises from reactions of Co to form iron carbides.

The surface area of Fe-Zn-Cu_3-K_6 was 160 m^2 g^{-1}, while surface areas after contact to synthesis gas for 25, 70 and 120 min were 31, 27, and 17 m^2 g^{-1}, consistent with the sintering of Fe-Zn-Cu_3-K_6 sample during Fe_3O_4 formation. The surface area also decreased slowly during the conversion of Fe_3O_4 to FeC_x. Besides, the surface area continuously decreased after FeC_x concentration reached 100 %, suggesting that the carbide-oxide transformations led to the sintering of particles during FTS reactions at 543 K. The activation process for ~60 min led to the highest CH_4 formation rates, suggesting that this is an optimal activation time at these conditions.

2.3.3. Effect of activation temperature and H_2/CO ratio on activation and FTS reactions.

Figure 2.5 shows FeC_x concentrations measured from *in situ* XAS on Fe-Zn-Cu_3-K_6 as a function of time at various temperatures (508, 523, 543, and 573 K). It is clear that at 543 and 573 K, FeC_x contributions approached constant values of ~100% after 60 min and 20 min, respectively. On the other hand, the FeC_x contributions at 508 and 523 K were ~80% and ~90% after 360 and 180 min, respectively. Figure 2.5 also shows the CH_4 formation rates measured at the same reaction condition as those used for the XAS experiments. The rate of CH_4 formation at 508 K and 523 K increased with increasing FeC_x content. At 543 and 573 K, the CH_4 formation rates increased with increasing FeC_x content and then the rates decreased with time on stream. At 573 K, deactivation evident after 5 min in contact with synthesis gas. It seems that the decrease of CH_4 formation rates was caused by the formation of the inactive species, such as carbon, upon exposure of iron oxides to synthesis gas at high temperature.

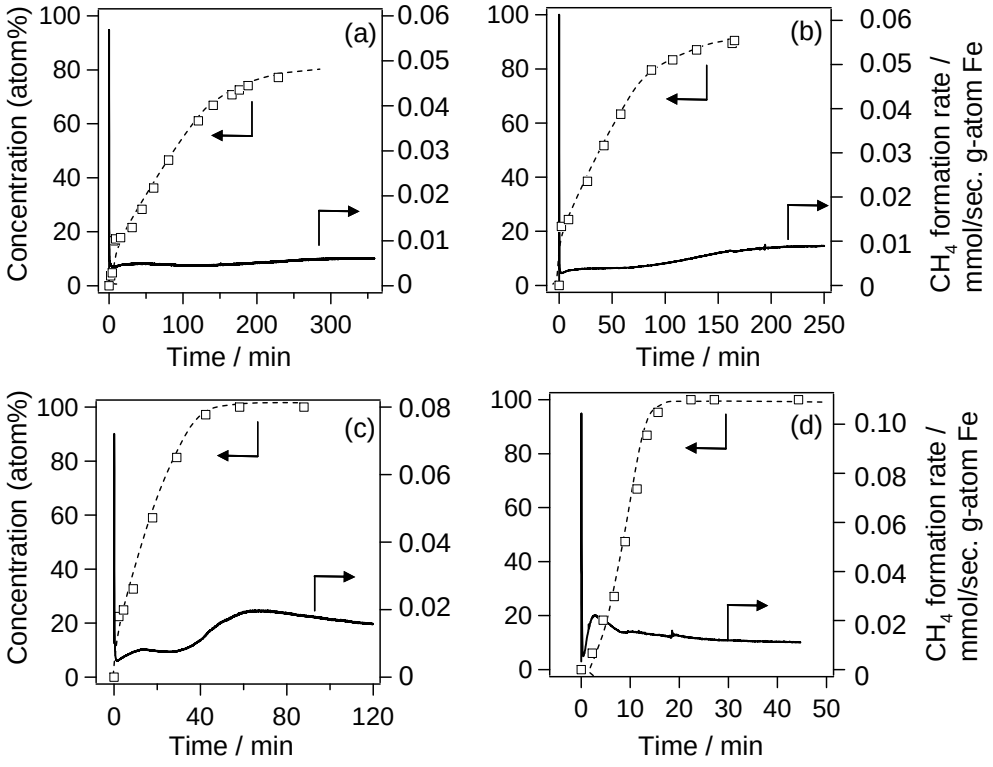

Figure 2.5. Fe carbide concentration (open mark) obtained from XAS (1 mg sample) and rate of CH_4 formation as a function of time on Fe-Zn-Cu_3-K_6 (0.2 g sample) at (a) 508, (b) 523, (c) 543, and (d) 573 K. (synthesis gas flow: 108 mol h^{-1} g-at Fe^{-1})

FTS rates increased with increasing reaction temperature. To evaluate the catalytic activities by the CH_4 formation rate, it is necessary to measure this rate and CH_4 formation rate at the same conditions after activation process. Table 2.1 summarizes the surface area of Fe-Zn-Cu_3-K_6 activated at various temperatures, as well as the CH_4 formation rates measured at 508 K after various activation processes. The activation processes at 543 K and 573 K were carried out for 70 and 5 min, respectively, because these times lead to maximum rates on Fe-Zn-Cu_3-K_6 at each of these temperatures (Figure 2.5). The surface area of Fe-Zn-Cu_3-K_6 samples activated at 508 K for 360 min was the lowest among all samples and the FeC_x concentration was ~80%. The relative surface area of the samples activated at lower temperatures (508, 523 K) is lower than those activated at higher temperature, even though the samples included Fe_3O_4 phases. Therefore it appears that the increase of activation temperature results in an increase in surface area. The activation at high temperature appears to lead to preferential nucleation at multiple locations and to smaller structures of Fe_2O_3 and Fe carbide.

Fe-Zn-Cu_3-K_6 samples activated at 508 K for 360 min showed the highest CH_4 formation rate among all catalysts. There are two possible basis for this observation. One is rapid catalyst deactivation at higher temperature. The contact of Fe-Zn-Cu_3-K_6 with synthesis gas at 573 K causes deactivation even after 5 min in spite of the low FeC_x concentration (20%) prevalent after this period of time. The other is that active sites formed via promoters depend on the location and effectiveness of these promoters. Cu and K species on Fe_2O_3 surface promote the reduction and carburization of Fe_2O_3. The reduction and carburization of Fe-Zn-Cu_3-K_6 at lower temperature occur by using H_2 and CO activated via promoters. The reduction and carburization by H_2 and CO activated via Fe_2O_3 itself, however, can also occur at higher temperature Therefore, it appears that the Fe-Zn-Cu_3-K_6 activated at lower temperature (523 K) appears to involve the beneficial effects of promoters near the active sites with consequent beneficial effects on the density and reactivity of active sites for the FT synthesis.

Table 2.1. Characterization results and CH_4 formation rate over Fe-Zn-Cu_3-K_6 activated at various temperature and time.

Temperature (K)	508	523	543	543	573	573
Activation time (min)	360	300	70	120	5	45
Surface area (m^2 g^{-1})[a]	12.1	14.6	26.9	16.8	42.5	31.3
FeC_x concentration (%)[b]	82	91	100	100	21	100
CH_4 formation rate (mmol s^{-1} g-at Fe^{-1})[c]	0.0060	0.0054	0.0052	0.0047	0.0039	0.0031

[a] Surface area measured after activation.

[b] FeC_x concentration measured after exposure to synthesis gas (1 mg Fe-Zn-Cu_3-K_6, H_2/CO=1, synthesis gas flow rate = 108 mol h^{-1} g-at Fe^{-1}).

[c] CH_4 formation rates measured at 508 K after activation (0.2 g Fe-Zn-Cu_3-K_6, H_2/CO=1, synthesis gas flow rate = 108 mol h^{-1} g-at Fe^{-1}).

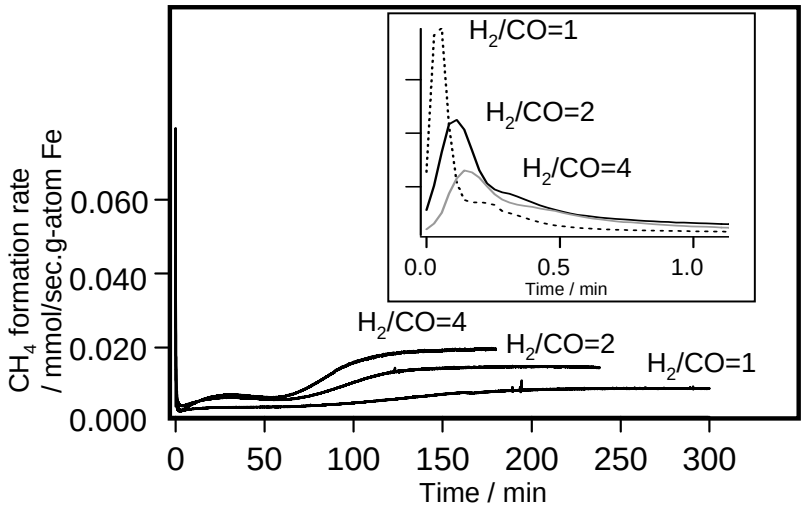

Figure 2.6. CH_4 formation rate on Fe-Zn-Cu_3-K_6 as a function of time under synthesis gas stream with various H_2/CO ratios at 523 K. (syngas flow: 108 mol h^{-1} g-at Fe^{-1}).

CH_4 formation rates of Fe-Zn-Cu_3-K_6 were measured to determine the effects of activation with gas mixtures with varying H_2/CO ratios. Figure 2.6 shows CH_4 formation rates on Fe-Zn-Cu_3-K_6 with such mixtures at 508 K. The increase of reactor temperature became small in the initial stage (~0.5 min) with increasing H_2/CO ratio and the sharp peak in that stage consequently became broad, suggesting that higher H_2/CO ratio led to slower rates of FeC_x formation at near-surface regions. Since CH_4 formation rates cannot be used to judge exposed site densities, because of the effects of H_2/CO ratios on intrinsic reaction rates, we have examined the effects of activation procedures by measuring surface areas and FTS rates at standard reaction conditions.

Figure 2.7 shows the surface area and CH_4 formation rate of Fe-Zn-Cu_3-K_6 at identical conditions (H_2/CO=1, 508 K, 0.1 MPa) after catalyst activation at 523 K under synthesis gas stream with different H_2/CO ratios. The CH_4 formation rate on Fe-Zn-Cu_3-K_6 activated with H_2/CO=1 was lower than on Fe-Zn-Cu_3-K_6 activated with H_2/CO=2. Fe-Zn oxide without promoters can be reduced to Fe_3O_4 by CO at 523 K, while it cannot be reduced by H_2. This implies that the CO-rich synthesis gas led to reduction by CO activated on Fe_2O_3 itself, but required reduction by H_2 activated on promoters. This reduction by CO activated via Fe_2O_3 causes a weakening of promoter effects on the rate of formation and the concentration of active species. On the other hand, Fe-Zn-Cu_3-K_6 activated at high H_2/CO ratioss (H_2/CO=4) gave the lowest CH_4 formation rates. It appears that this case also brings about the lack of promoter because of the relatively rapid active site formation irrespective of the presence or absence of promoter components. Fe-Zn-Cu_3-K_6 samples activated with stoichiometric synthesis gas (H_2/CO=2) gave the highest CH_4 formation rate among all catalysts.

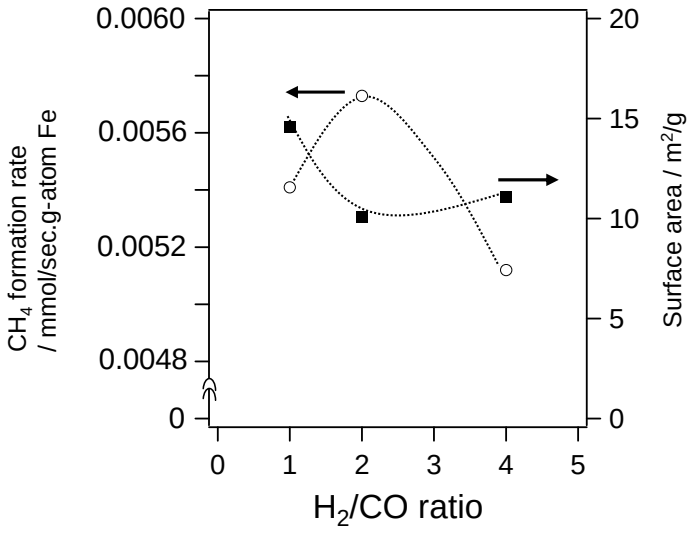

Figure 2.7. Surface area and CH_4 formation rate at 508 K and 0.1 MPa under synthesis gas flow (H_2/CO=1) after catalyst activation at 523 K under synthesis gas flow with various H_2/CO ratios. (Fe-Zn-Cu_3-K_6; syngas flow rate: 108 mol h^{-1} g-at Fe^{-1}).

FTS rates and selectivities were measured on Fe-Zn-Cu_3-K_6 samples with hydrogen-poor synthesis gas (H_2/CO=1) reactant after catalyst activation with stoichiometric synthesis gas (H_2/CO=2) reactant at 508 K and three flow rates (21.6, 54.0, 108 mol/h.g-atom Fe). The highest flow rate (108 mol h^{-1} g-at Fe^{-1}) was the same as that used on the transient FTS experiments reported above. Table 2.2 summarizes the steady-state performance of Fe-Zn-Cu_3-K_6 activated at 508 K at these synthesis gas flow rates. Table 2.2 also shows the steady-state performance of Fe-Zn-Cu_3-K_6 activated using conventional methods [1]. Decreasing reactant flow rates during activation process led to higher hydrocarbon formation rates. Hydrocarbon formation rates on Fe-Zn-Cu_3-K_6 activated with stoichiometric synthesis reactants (H_2/CO=2, flow rate 21.6 mol h^{-1} g-at Fe^{-1}) at 508 K was higher compared than on catalysts activated with other compositions. Fe-based catalysts are typically activated above 573 K. Our study suggests that lower reactor temperature can be sufficient to activate catalysts and lead to the improved FTS catalyst performance.

Table 2.2. Steady-state FTS performance of Fe-Zn-Cu_3-K_6 activated at several conditions. (H_2/CO=1, 508 K, 2.14 MPa, CO conversion 29-32 %).

Activation Temperature (K)	543	508	508	508
Flow rate (mol h^{-1} g-at Fe^{-1})[a]	21.6	21.6	54.0	108
Steady-state performance				
CO_2 selectivity (%)	29.5	35.3	34.6	31.4
CH_4 selectivity (%)[b]	4.9	4.8	4.1	3.9
C_{5+} selectivity (%)[b]	86.1	88.3	90.2	90.2

HC formation rate (mol CO/h.g-at. Fe)	6.31	7.08	6.89	6.54

[a] Synthesis gas (H_2/CO=2).
[b] CH_4 and C_{5+} selectivities are reported on a CO_2-free basis.

3. Mechanism and kinetics of the Fischer-Tropsch synthesis on Fe-based catalysts.

The detailed kinetics and reaction mechanism of the Fischer-Tropsch synthesis (FTS) were also addressed as part of this project. Kinetic measurements were performed on a Fe-Zn-Cu_3-K_6 catalyst, which was found to be the most active material among those developed as part of this study. The ultimate objective of these experiments is to propose a reaction mechanism that describes and predicts the formation rates of various hydrocarbons formed during reactions of CO and H_2 on Fe-based catalysts and which can be used to embed into hydrodynamic models of complex practical reactors.

3.1. Influence of reactants partial pressure on hydrocarbon formation rate.

The rates of CO conversion to hydrocarbons (HC) as a function of the CO conversion at different inlet CO and H_2 partial pressures are shown in Figures 3.1 and 3.2 respectively. These data were obtained by changing the CO space velocity while keeping t the reaction temperature (508 K) and all other pressures constant. The rates of CO conversion to hydrocarbon decreased with increasing CO conversion in all experiments, probably as a result of the depletion of reactants. The decrease of the CO conversion rate to hydrocarbons with increasing CO conversion may also reflect inhibition effects caused by competitive adsorption of water formed during FTS reactions [17]. It has been shown in the literature that the rate of FTS is not inhibited by the addition of water with the syngas feed for H_2O/CO ratios less than 0.3 [18]. Under our reactions conditions, the water-to-carbon monoxide ratio inside the catalytic bed was below 0.3 at all reaction conditions.

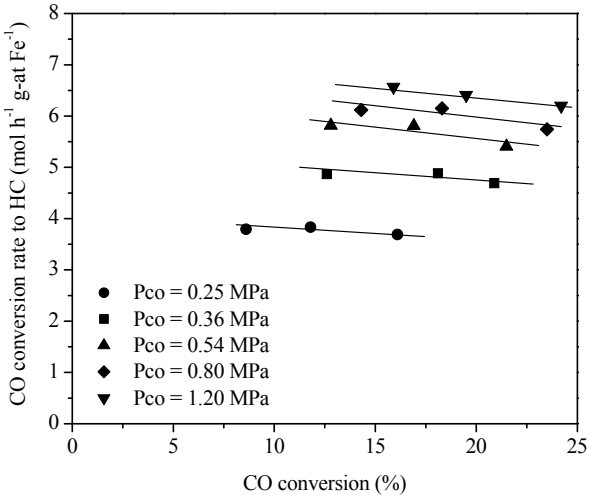

Figure 3.1. CO conversion rate to hydrocarbons as a function of CO conversion at different inlet CO partial pressures (H_2=1.20 MPa).

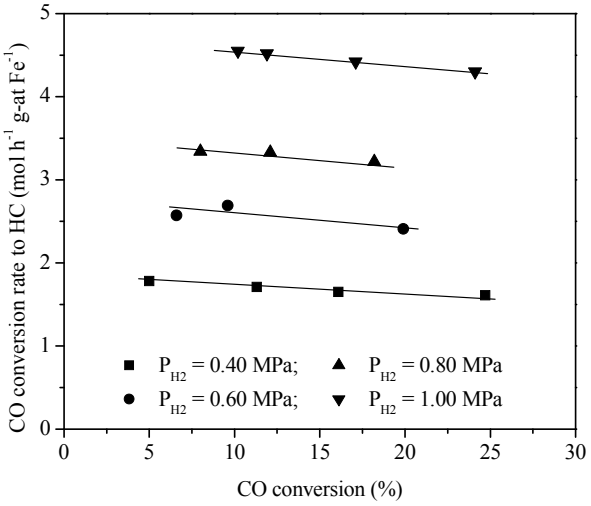

Figure 3.2. CO conversion rate to hydrocarbons as a function of CO conversion at different inlet H_2 partial pressures (CO=0.40 MPa).

Figure 3.3 shows the rate of CO conversion to hydrocarbons extrapolated at zero CO conversion level at different CO and H_2 pressures. The reaction rate is approximately first order in CO at low CO inlet partial pressures, but becomes almost zero order at higher CO pressures. The reaction orders with respect to CO reported in the literature are between -0.5 and +0.5 [4,19,20]. In contrast, CO conversion rates to hydrocarbon increased linearly with increasing H_2 pressure (0.4-1.0 MPa.

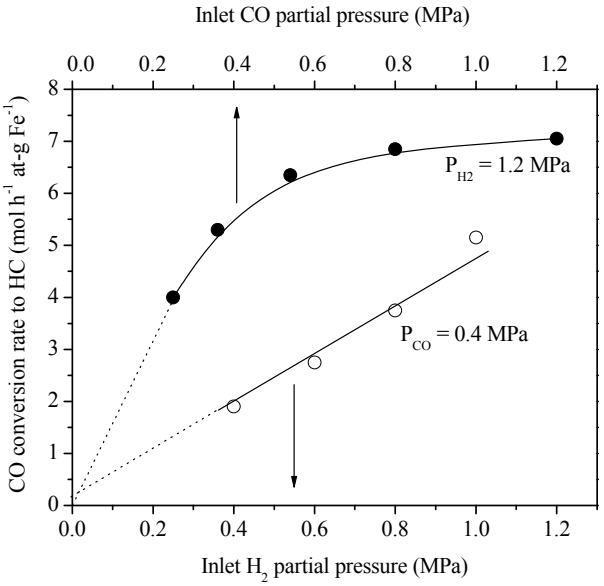

Figure 3.3. Effect of CO and H_2 partial pressures on the CO conversion rate to hydrocarbon extrapolated a zero CO conversion.

3.2. CO_2/H_2O formation and oxygen removal selectivity.

Water-gas shift (WGS) is a reversible reaction that approaches equilibrium with increasing residence time and temperature during FTS reactions. This approach to equilibrium and its kinetic consequences can be rigorously described by a parameter η:

$$\eta = \frac{1}{K_{WGS}} \cdot \frac{P_{CO_2} P_{H_2}}{P_{CO} P_{H_2O}} \qquad (3.1)$$

where P_i is the partial pressure of species *i* and K_{WGS} is the equilibrium constant for the WGS at the prevalent FTS reaction temperature. The values of η increase from 0 to 1 as WGS reaction approach equilibrium. It has been previously shown that [7]:

$$r = r_f - r_r = r_f(1-\eta) \qquad (3.2)$$

where r, r_f and r_r are respectively the net, forward and reverse rate of CO_2 formation. This expression was used here to calculate the rate of forward CO_2 formation at various H_2 and CO pressures.

Figure 3.4 shows the forward rate of CO_2 formation as a function of the CO conversion at different inlet CO partial pressures. These data were obtained by changing the CO space velocity at constant temperature (508 K) and H_2 partial pressure (1.20 MPa). The forward rate of CO_2 formation increases with increasing CO conversion and CO pressure. The effect of CO conversion reflects the formation of CO_2 via secondary WGS reactions. The slope of CO_2 formation rate with residence time reflects the rate of secondary WGS reactions and increase slightly with increasing inlet CO pressure. The forward rate of CO_2 formation extrapolated to zero CO conversion levels are non-zero at all conditions, consistent with the primary formation of CO_2 *via* reactions of chemisorbed carbon monoxide (CO*) and oxygen (O*) (CO* + O* → CO_2). It is evident from these data that the main effect of increasing inlet CO partial pressures on CO_2 formation pathways is to enhance the rate of primary CO_2 formation. Figure 3.5 depicts the rate of primary CO_2 formation as a function of the inlet CO partial pressure. The rate of primary CO_2 formation increases linearly at low CO partial pressure. On the contrary, this rate is almost zero-order in CO at higher CO partial pressures.

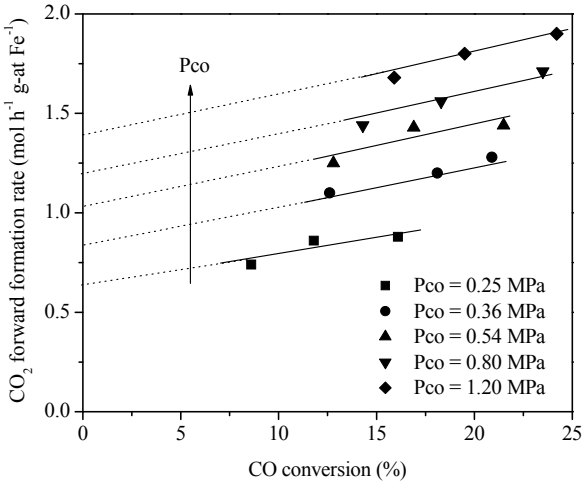

Figure 3.4. Rate of forward CO_2 formation as a function of CO conversion at different inlet CO pressures (H_2=1.20 MPa).

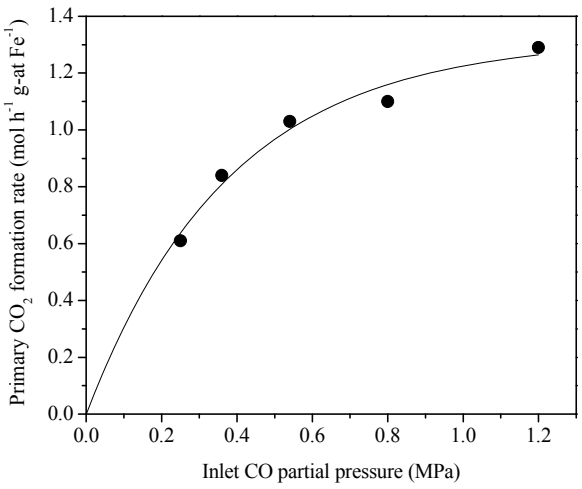

Figure 3.5. Rate of primary CO_2 formation as a function of inlet CO partial pressure (H_2=1.20 MPa).

Figure 3.6 shows the forward rate of CO_2 formation as a function of CO conversion for different inlet H_2 partial pressures. As described above, the forward rate of CO_2 formation increased with increasing CO conversion. However, the intercept with the y-axis at zero CO conversion level and the slopes of the rate of forward CO_2 formation are independent of inlet H_2 pressures, suggesting that H_2 pressures do not affect the rate at which oxygen from CO is removed as CO_2 via primary reactions or secondary WGS. Figure 3.7 shows clearly that the rate of primary CO_2 formation is independent on the inlet H_2 partial pressure.

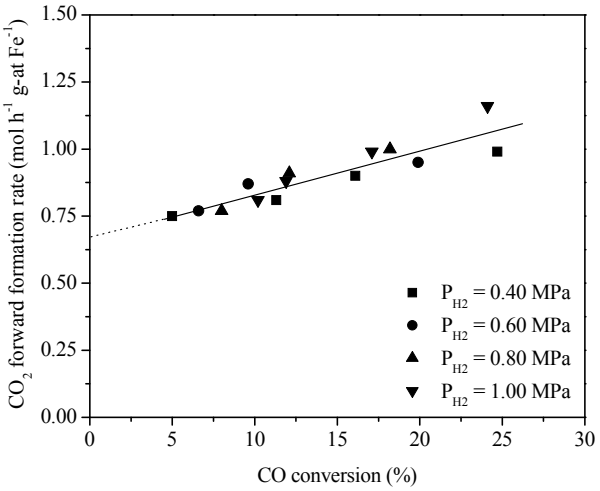

Figure 3.6. Forward rate of CO_2 formation as a function of CO conversion at different inlet H_2 partial pressures (CO=0.40 MPa).

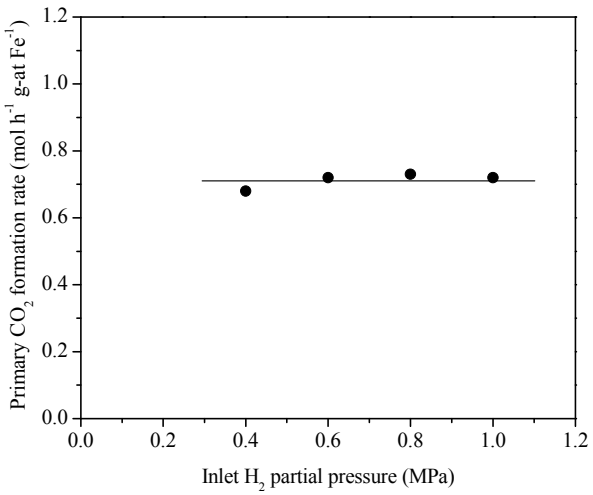

Figure 3.7. Rate of primary CO_2 formation as a function of the inlet H_2 partial pressure (CO=0.40 MPa).

The dependence of the rate of forward CO_2 formation on the mean CO_2 pressure in the reactor was also examined in our experiments (Figure 3.8). The forward rate of CO_2 formation was unaffected by the prevalent CO_2 pressure within the reactor. The forward and net rates of carbon dioxide formation are almost identical because WGS reaction is far from the equilibrium (η_{max}=0.105) under our reaction conditions. This means that added CO_2 was not significantly converted to CO *via* the reverse water-gas shift reaction ($CO_2 + H_2 \leftrightarrows CO + H_2O$) during these experiments.

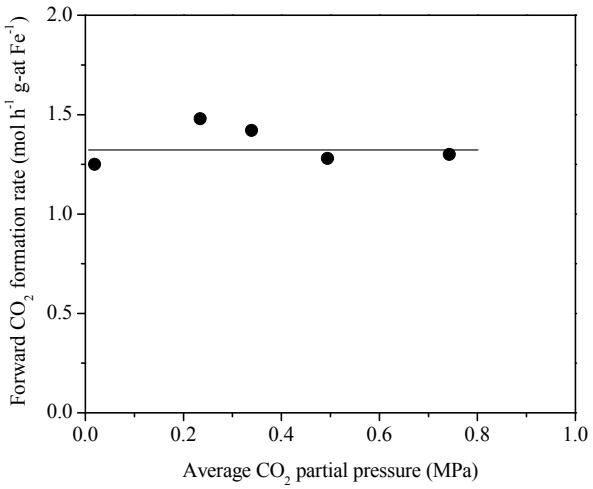

Figure 3.8. Forward rate of CO_2 formation as a function of the average CO_2 partial pressure (P_{CO}=H_2=0.75 MPa).

3.3. Fischer-Tropsch synthesis mechanism on Fe-based catalysts.

The analysis of the observed kinetic dependence of the rate of hydrocarbons and primary CO_2 formation on the reactants partial pressures led us to propose the following set of elementary steps for FTS:

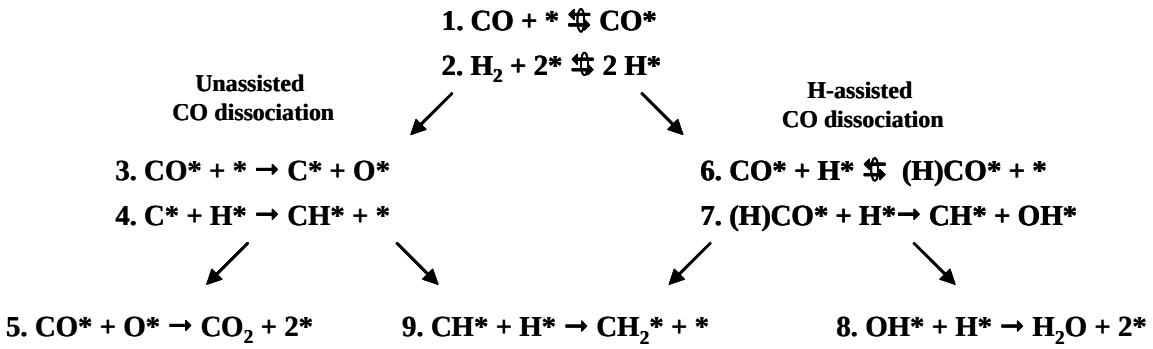

Scheme 3.1. Proposed elementary steps for Fischer-Tropsch synthesis on Fe catalysts.

The first step describes the molecular non-activated adsorption of carbon monoxide [21]. The dissociative adsorption of hydrogen (step 2) requires two vacant active sites, typically on surfaces nearly saturated with chemisorbed CO. Both steps are typically assume to be equilibrated because of their low activation barriers and modest exothermic enthalpies of adsorption. The dissociation of adsorbed CO species (CO*) can occur via two independent pathways – unassisted dissociation and H-assisted dissociation. In the unassisted route, CO* species cleave their C-O bonds directly to form surface carbon (C*) and oxygen (O*) species using a vicinal empty site (step 3). The C* species are then hydrogenated to form CH* species (step 4) and ultimately monomers for chain growth. Surface O* species are removed exclusively by reaction with CO* to produce primary carbon dioxide (step 5). It would be reasonable to consider that O* species can also be stepwise hydrogenated to form water. Parallel density functional theory calculations and the comparison with data discussed below indicate that the first hydrogenation step (O* + H* → OH*) requires, however, a very high activation energy, and consequently, surface O* species are preferential removed as CO_2. In assisted routes, CO* dissociation occurs also with the participation of H* species (H-assisted route). Thus, CO* species first react with H* to form hydrogenated CO* species (step 6). Next, these species are dissociated with the participation of H* to form surface CH* and OH* groups (step 7). These OH* groups are the hydrogenated to form water (step 8) [22,23], while hydrogenation of the CH* species formed in steps 4 and 7 leads to the surface FTS monomers, CH_2* (step 9).

3.4. Kinetic analysis of the Fischer-Tropsch Synthesis with Fe-based catalysts.

The following rate expression can be derived from the reaction mechanism presented in Scheme 3.1:

$$r_{HC} = \frac{K_1 K_2 K_6 k_7 P_{H_2} P_{CO}}{(1 + K_1 P_{CO})^2} + \frac{K_1 k_3 P_{CO}}{(1 + K_1 P_{CO})^2} \qquad (3.3)$$

This rate equation was derived by assuming that: (*i*) adsorption of hydrogen and carbon monoxide are *quasi*-equilibrated with their gas phase concentrations (9); (*ii*) CO is adsorbed much more strongly than H_2 and chemisorbed CO is therefore the most abundant surface species along with free sites [6]; (*iii*) the concentrations of all intermediates on the catalyst surface are at steady-state; and (*iv*) catalytic sites for hydrocarbons formation are uniform and homogeneously distributed (Langmuirian surface assumption) [24].

This rate expression reflects the formation of hydrocarbons from CO activated via the two proposed routes. The first term represent the formation of hydrocarbon *via* the H-assisted pathway, while the second term corresponds to the unassisted route. According to the FTS mechanism here proposed, the first term in Equation 3.3 also reflects the rate of water formation, because oxygen rejection occurs exclusively as water in assisted pathways, while the second term denotes the rate of primary CO_2 formation, because of its exclusive role as the oxygen rejection route in assisted pathways. Therefore, the relative rate of oxygen removal as H_2O or CO_2 is given by:

$$\frac{r_{H_2O}}{r_{CO_2}} = \frac{K_2 K_6 k_7}{k_3} \cdot P_{H_2} \qquad (3.4)$$

According to this expression, the ratio r_{H_2O} / r_{CO_2} should be first order with respect the H_2 pressure and independent on the CO pressure. This is in contrast with the prediction obtained from the classical FTS mechanism, which predicts a markedly different behavior. Figure 3.9 shows that measured data agree well with the predictions of our proposed mechanism and with the form of Equation 3.4. The relative importance of assisted and unassisted CO dissociation pathways on the rate of hydrocarbon formation is therefore given by the r_{H_2O} / r_{CO_2} ratio, because the rate of water formation (r_{H_2O}) reflects the extent of the H-assisted CO dissociation pathway, while the rate of CO_2 formation (r_{CO_2}) corresponds to the rate of unassisted pathways. Figure 3.9 shows that both CO activation pathways occur concurrently on Fe surfaces, although the hydrogen-assisted CO dissociation steps prevail prevails over unassisted paths at hydrogen partial pressures typical for commercial FTS practice (1-3 MPa).

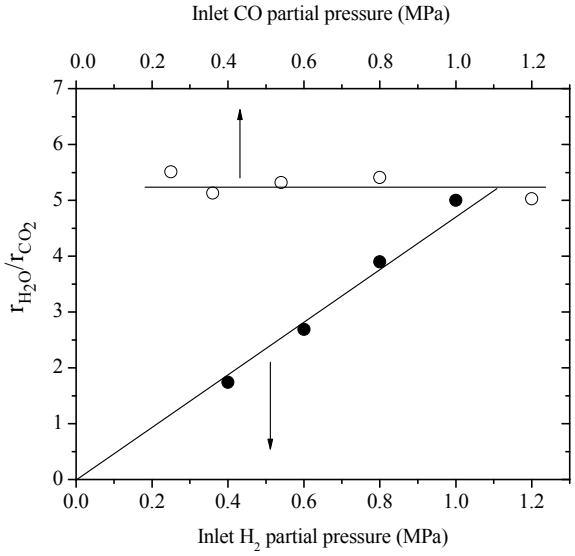

Figure 3.9. Oxygen removal selectivity (r_{H_2O} / r_{CO_2}) as a function of CO and H_2 partial pressures.

Table 3.1 shows the kinetic analysis of FTS and oxygen rejection pathways based on our data and proposed elementary steps. A nonlinear regression method was used in order to fit the experimental data to the different rate expressions. The model parameters were calculated from

the experimental data by using Levenberg-Marquardt steepest descent methods and all the reaction rate data available. It is observed that the kinetic parameters ($K_1K_2K_6k_7$ and K_1k_3) obtained from different and independent measurements are in agreement, consistent with the accuracy and validity of the FTS mechanism here proposed. The equilibrium constant for the CO adsorption process (K_1) can be calculated from the kinetic parameters in Table 3.1. We have found that K_1=0.77±0.14 MPa^{-1}, which resembles the value reported by van der Laan and Beenackers [25] on Fe-Cu-K-SiO_2 catalysts at 523 K.

Table 3.1. Rate expressions and parameters for the FTS kinetic model.

Rate Expression	$K_1K_2K_6k_7$ (mol h^{-1} at-g Fe^{-1} MPa^{-2})	K_1k_3 (mol h^{-1} at-g $Fe^{-1}MPa^{-1}$)
$r_{HC} = \frac{K_1K_2K_6k_7 P_{CO}P_{H2} + K_1k_3 P_{CO}}{(1+K_1P_{CO})^2}$	16.05 ± 1.04	2.70 ± 0.44
$r_{H_2O} = \frac{K_1K_2K_6k_7 P_{CO}P_{H2}}{(1+K_1P_{CO})^2}$	15.68 ± 1.59	-
$r^{p}_{CO_2} = \frac{K_1k_3 P_{CO}}{(1+K_1P_{CO})^2}$	-	3.47 ±0 .82

Figure 3.10 compares the experimental and model-predicted hydrocarbon formation rates. The reaction rate calculated with the kinetic expressions derived from our model is in good agreement with the measured rate data again consistent with the accuracy and validity of the elementary steps proposed and with the assumptions made in extracting the functional forms of the reaction rate equations.

In conclusion, the FTS mechanism proposed in this work contemplates the possibility of parallels pathways for CO activation over Fe-based catalysts. An indirect consequence from this mechanism is that oxygen atom removal pathways as water or carbon dioxide take place simultaneous and independently.

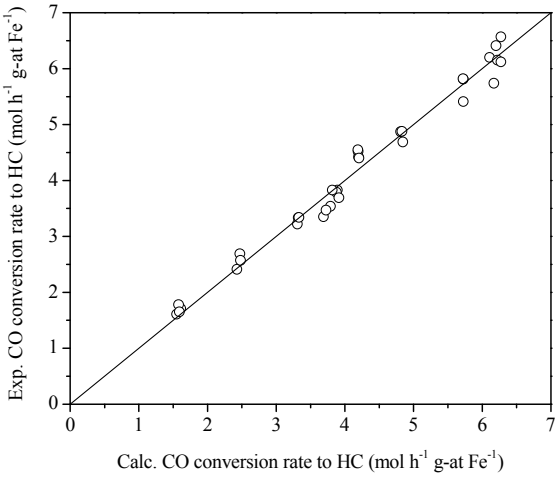

Figure 3.10. Parity plot for the experimental and calculated CO conversion rate to hydrocarbons.

The concentration of water in the gas phase increases with CO conversion levels. Our mechanism would then suggest that water molecules can be readsorbed onto active sites and influence potentially reaction rates. As OH* concentration increases, the step in the mechanism that forms CH* and OH* species (step 7 in Scheme 3.1) becomes reversible and position of its thermodynamic equilibrium less favorable. Since the step preceding this one is *quasi*-equilibrated, this means that some of the CO* species can have another opportunity to react either with adsorbed hydrogen (H*) or with a vacant active site (*) to form surface carbon (C*) and oxygen atoms (O*), which can then react with another CO* species to produce carbon dioxide. In summary, this reaction pathway is able to oxidize CO to CO_2 using water, which is in fact the reaction known as the water-gas shift. We have found, therefore, a reaction mechanism for FTS with some elementary steps in common with WGS reaction and the mechanism for the latter is in fact contained within the catalytic sequences proposed herein for FTS.

These results have been confirmed with theoretical calculations about the Fischer-Tropsch Synthesis mechanism. This work has been done in close collaboration with Prof. Manos Mavrikakis, from the University of Wisconsin, Madison. From these DFT calculations, we have demonstrated that the H-assisted CO dissociation pathway is energetically favored on a Fe(110) surface. Moreover, we have determined that the most probable intermediates are surface formyl species. These calculations and results support our hypothesis about the importance of the assistance of hydrogen species (H*) in the CO dissociation event. We have also found that the unassisted CO cleavage also takes place to some extent. Therefore, this is in accordance with the experimental observation consisting in the formation of primary carbon dioxide, which is produced *via* the unassisted CO pathway. The results of this collaboration, which was not funded by this project, will be published within the next six months.

3.5. Kinetic H_2/D_2 isotope effects on Fe-based catalysts.

3.5.1. H_2/D_2 effect on hydrocarbon formation rate.

During this project, we have also analyzed the consistency between the proposed mechanism and the H_2/D_2 kinetic isotope effects (r_H/r_D) measured on iron-based Fischer-Tropsch catalysts

(Fe-Zn-K-Cu). The reaction mechanism proposed for FTS contains the two parallel pathways for CO activation on Fe-based catalysts. On one hand, adsorbed carbon monoxide species (CO*) can be directly dissociated to form surface carbon atoms (C*) which can be subsequently hydrogenated to produce the FTS monomers (CH_2*). But at the same time, hydrogenation of undissociated carbon monoxide molecules leads also to the formation of surface monomers. Although both monomer formation routes occur simultaneously over the catalyst surface, our results showed that the hydrogen-assisted CO dissociation mechanism is predominant at typical H_2 and CO partial pressures. According to this mechanism, dihydrogen and hydrogen atoms formed *via* its dissociation are involved in all proposed elementary steps, except for the unassisted CO dissociation. Therefore, kinetic deuterium isotope effects could be used as a probe of these kinetically relevant steps and to provide evidence for or against a specific mechanistic proposal because the rate constant for the reaction of the hydrogen compound (k_H) differs of that obtained for the same reaction with the corresponding deuterium compound (k_D) when a bond to hydrogen or deuterium is formed or broken in the kinetically-relevant steps of a reaction. On the other hand, the thermodynamic deuterium isotope effect, namely, the effect of isotopic substitution on the equilibrium constant, can be used to indicate important characteristics of reaction equilibriums. Therefore, comparisons of rates and selectivities for reactions of H_2/CO and D_2/CO mixtures on iron-based catalysts can provide specific evidence about the nature of the kinetically-relevant steps.

Figure 3.11 shows the CO conversion rate to hydrocarbons as a function of the CO conversion level. It can be clearly seen that hydrocarbons formation rate is higher (about two times) when D_2/CO reactants mixture is used instead of H_2/CO reactants. It is also noted that hydrocarbon formation rate decreases when the CO conversion is increased for both reactant mixtures.

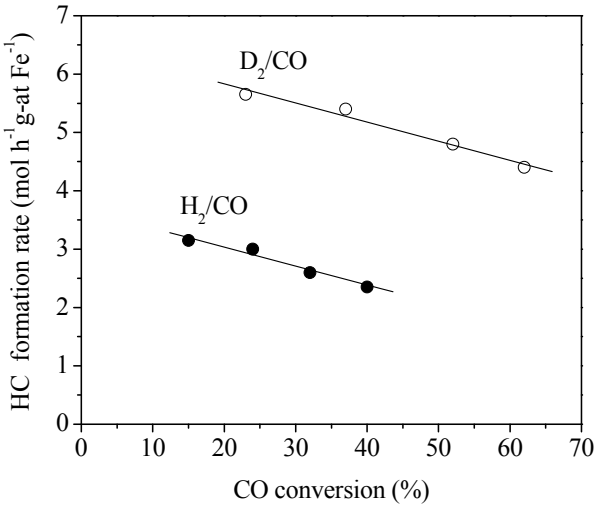

Figure 3.11. Hydrocarbon formation rates as a function of CO conversion for H_2/CO or D_2/CO reactants (Zn/Fe=0.1, K/Fe=0.02, Cu/Fe=0.01) at 508 K and 2.14 MPa.

We have previously shown that the CO conversion rate to hydrocarbon is given by:

$$r_{CH_2} = \frac{K_1 K_2 K_3 k_4 P_{CO} P_{H_2}}{(1 + K_1 P_{CO})^2} + \frac{K_1 k_5 P_{CO}}{(1 + K_1 P_{CO})^2} \qquad (3.5)$$

where r_{CH_2} is the CO conversion rate to hydrocarbons, k_i is the rate constant for step *i*, and K_i is the equilibrium constant for step *i*. The use of D_2 instead of H_2 has no influence on the second term in Eq. 3.5. The observed kinetic isotope effect is, therefore, the combination of the individual effects of hydrogen or deuterium use on K_2, K_6 and k_7. Thus, the KIE is proportional to:

$$\mathrm{KIE} = \frac{r_{CH_2}}{r_{CD_2}} \propto \frac{K_2^H K_6^H k_7^H}{K_2^D K_6^D k_7^D} = \frac{K_2^H}{K_2^D} \cdot \frac{K_6^H}{K_6^D} \cdot \frac{k_7^H}{k_7^D} \qquad (3.6)$$

where r_{CH_2} and r_{CD_2} are respectively the rate of hydrocarbon formation obtained with H_2/CO and D_2/CO. The superscripts of the rate and equilibrium constants denote their provenance from the two respective reactant mixtures. The observed isotope effect results, in turn, from the combination of equilibrium (K_2 and K_6) and kinetic (k_7) isotope effects.

Rate and equilibrium constants within statistical mechanics formalism can be described as:

$$K = \frac{\prod_j Q_p^{\nu_j}}{\prod_i Q_r^{\nu_i}} \quad \text{and} \quad k = \frac{k_B T}{h} \frac{Q^{\Xi}}{\prod_i Q_r^{\nu_i}} \qquad (3.7)$$

where (kT/h) is a frequency factor; Q_r, Q_p and Q^{Ξ} are the partition functions for reactants, products, and transition state complexes; and ν_i and ν_j are the stoichiometric coefficients for reactants *i* and products *j*. Therefore, the equilibrium isotope effect for H_2 (D_2) chemisorption is given by the following expression:

$$\frac{K_2^H}{K_2^D} = \left(\frac{Q_{D_2}}{Q_{H_2}}\right) \cdot \left(\frac{Q_{H^*}}{Q_{D^*}}\right)^2 \qquad (3.8)$$

Each ratio of the partition functions can be evaluated as a combination of the translational, rotational, vibrational and the electronic partition functions, and the equilibrium kinetic isotope effect can be evaluated to be:

$$\frac{K_2^H}{K_2^D} = \left(\frac{Q_{D_2}}{Q_{H_2}}\right) \cdot \left(\frac{Q_{H^*}}{Q_{D^*}}\right)^2 = 5.68 \cdot e^{\left[\left(E_{H_2} - 2E_{H^*}\right) - \left(E_{D_2} - 2E_{D^*}\right)\right]/RT} \qquad (3.9)$$

The equilibrium isotope effect for H_2 and D_2 (K_2^H / K_2^D) depends on the relative chemisorption enthalpies of hydrogen and deuterium on Fe surfaces. Soller *et al.* [26] observed about 1.4 times more adsorption of D_2 than H_2 on Cu powder at 398 K. Larger adsorption coefficients were measured for D_2 than for H_2 also on Ni samples [27,28]. In the case of Fe catalysts, previous studies have indicated that chemisorption of D_2 is preferred over that of H_2 [29]. Although we have not measured the relative coverage of hydrogen and deuterium atoms, indirect evidence of the larger deuterium coverage is derived from the lower olefin-to-paraffin ratios obtained when D_2/CO mixture was used, which suggests a relatively higher surface coverage of deuterium atoms, i.e., $\theta_{D^*} > \theta_{H^*}$. It is expected, therefore, that $K_2^H / K_2^D < 1$.

It can be shown that the equilibrium isotope effect for the formation of the formyl intermediates (HCO* or DCO*) is given by the following expression:

$$\frac{K_6^{\mathrm{H}}}{K_6^{\mathrm{D}}} = \left(\frac{Q_{\mathrm{D}*}}{Q_{\mathrm{H}*}}\right)\cdot\left(\frac{Q_{\mathrm{HCO}*}}{Q_{\mathrm{DCO}*}}\right) \approx \mathrm{e}^{\left(E_{(\mathrm{H}*-E_{\mathrm{D}*}}\right)/\mathrm{RT}} \cdot \mathrm{e}^{\left(E_{\mathrm{DCO}*}-E_{\mathrm{HCO}*}\right)/\mathrm{RT}} = \mathrm{e}^{\left[\left(E_{\mathrm{DCO}*}-E_{\mathrm{D}*}\right)-\left(E_{\mathrm{HCO}*}-E_{\mathrm{H}*}\right)\right]/\mathrm{RT}} \qquad (3.10)$$

Previously studies conducted by Ozaki [30] revealed that the equilibrium constant for the addition of deuterium to an adsorbed species is generally larger than that for the addition of hydrogen. Therefore, the ratio of equilibrium constants for the formation of formyl species, $K_6^{\mathrm{H}} / K_6^{\mathrm{D}}$, should be lower than unity.

The kinetic isotope effect for the hydrogen-assisted HCO* species dissociation (step 7) is therefore predicted to be given by:

$$\frac{k_7^{\mathrm{H}}}{k_7^{\mathrm{D}}} = \left(\frac{Q^{\Xi}_{\mathrm{CH}*\mathrm{OH}*}}{Q^{\Xi}_{\mathrm{CD}*\mathrm{OD}*}}\right)\cdot\left(\frac{Q_{\mathrm{D}*}}{Q_{\mathrm{H}*}}\right)\cdot\left(\frac{Q_{\mathrm{DCO}*}}{Q_{\mathrm{HCO}*}}\right) \approx \mathrm{e}^{\left(E^{\Xi}_{\mathrm{CD}*\mathrm{OD}*}-E^{\Xi}_{\mathrm{CH}*\mathrm{OH}*}\right)/\mathrm{RT}} \cdot \mathrm{e}^{\left(E_{(\mathrm{H}*-E_{\mathrm{D}*}}\right)/\mathrm{RT}} \cdot \mathrm{e}^{\left(E_{\mathrm{HCO}}-E_{\mathrm{DCO}*}\right)/\mathrm{RT}} =$$

$$= \mathrm{e}^{\left[\left(E^{\Xi}_{\mathrm{CD}*\mathrm{OD}*}-E_{\mathrm{DCO}*}-E_{\mathrm{D}*}\right)-\left(E^{\Xi}_{\mathrm{CH}*\mathrm{OH}*}-E_{\mathrm{HCO}*}-E_{\mathrm{H}*}\right)\right]/\mathrm{RT}} \qquad (3.11)$$

Ozaki studied also the kinetic isotope effect for reactions involving the addition of hydrogen, concluding that $k^{\mathrm{H}} > k^{\mathrm{D}}$ in most cases. This is the result of the differences in the zero-point energies of deuterated and hydrogenated species, which is the primary origin of the effect. For kinetic isotope effects, we can assume that the step 4 in Scheme 1 is faster when H_2/CO synthesis gas is used ($k_7^{\mathrm{H}} > k_7^{\mathrm{D}}$).

In conclusion, the overall inverse isotope effect ($r_H/r_D<1$) for hydrocarbon formation indicates that hydrogen-containing species are involved in kinetically relevant steps. Moreover, the observed isotope effect is the result of the combination of kinetic and thermodynamic isotope effects. Since $r_H/r_D<1$, we can conclude that the thermodynamic isotope effects dominate the values measured for FTS reactions on representative Fe-based catalysts in this study.

3.5.2. H_2/D_2 effect on CO_2 formation rate

Figure 3.12 shows the rate of carbon dioxide formation as a function of CO conversion at 508 K and 2.14 MPa total pressures with H_2/CO and D_2/CO (2/1 molar ratio). CO_2 formation rates extrapolated to low CO conversion levels are non-zero, consistent with the primary nature of pathways for removal of oxygen as carbon dioxide (step 5 in Scheme 3.1) [7]. The primary CO_2 formation rate is similar for H_2/CO and D_2/CO reactants, implying that the nature of syngas (H_2/CO or D_2/CO) did not influence the rate of oxygen removal as carbon dioxide. According to the reaction mechanism depicted in Scheme 3.1, the primary carbon dioxide formation rate is given by:

$$\mathrm{r}^{\mathrm{p}}_{\mathrm{CO}_2} = \frac{K_1 k_3 \mathrm{P}_{\mathrm{CO}}}{(1+K_1\mathrm{P}_{\mathrm{CO}})^2} \qquad (3.12)$$

According to Equation 3.12, the formation of the carbon dioxide through primary pathways is not influenced by the use of H_2/CO or D_2/CO, in agreement with the experimental results. The isotopic content of the reactants, however, does affect the rate of carbon dioxide formation via secondary reactions, as expected from the involvement of OH* and OD* species in such reaction pathways.

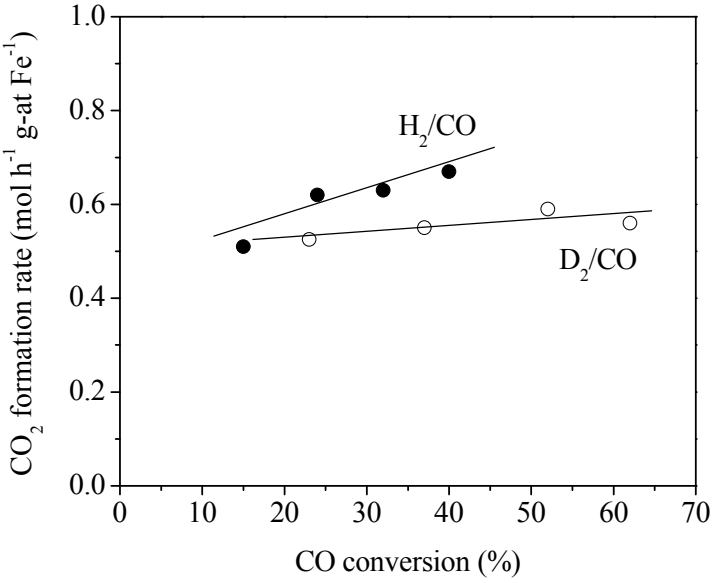

Figure 3.12. CO_2 formation rate as a function of CO conversion for H_2/CO or D_2/CO reactants (Zn/Fe=0.1, K/Fe=0.02, Cu/Fe=0.01) at 508 K and 2.14 MPa.

3.5.3. Ratio of hydrocarbon formation rates (r_H/r_D)

The kinetic isotope effect can be expressed by the ratio r_H/r_D, where r_H and r_D are the rates of hydrocarbon formation rates H_2/CO and D_2/CO reactants, respectively. Since we do not have experimental values for both r_H and r_D at the same CO conversion, we have calculated the r_H values by interpolation of rate *vs.* CO conversion to obtain values of r_D. Similarly, we have also obtained a fitted value of r_D for each experimental value of r_H. Figure 3.13 shows the r_H/r_D ratio for the rates of CO conversion and hydrocarbon and CO_2 formation at different CO conversion levels.

The r_H/r_D ratio for the hydrocarbon formation is about 0.5 at low CO conversion values. We believe that the inverse isotope effect for the hydrocarbon formation ($r_H/r_D<1$) is related to the higher surface coverage of D* when compared to H*. The KIE decreases slightly with increasing CO conversion. This decrease could be a consequence of the lower average hydrogen partial pressure as the CO conversion increases. Hydrogen and deuterium partial pressures decrease slightly with increasing CO conversion. We speculate that surface hydrogen concentration (θ_{H*}) is more sensitive to the reduction of the H_2 pressure than the surface deuterium coverage (θ_{D*}) because the adsorption coefficient of D_2 is higher than the adsorption coefficient of H_2. Accordingly, the rate of hydrocarbon formation decreases faster when H_2/CO is used, and consequently, the r_H/r_D ratio for hydrocarbon formation decreases with increasing CO conversion (Figure 11).

The r_H/r_D ratio for the rate of CO_2 formation is greater than 1 (Figure 3.13) and it increases with CO conversion. The normal kinetic isotope effect for CO_2 formation rates ($r_H/r_D>1$) reflects the higher energy required for the cleavage of the C-D bond relative to the C-H bond in the intermediates required for secondary WGS reactions.

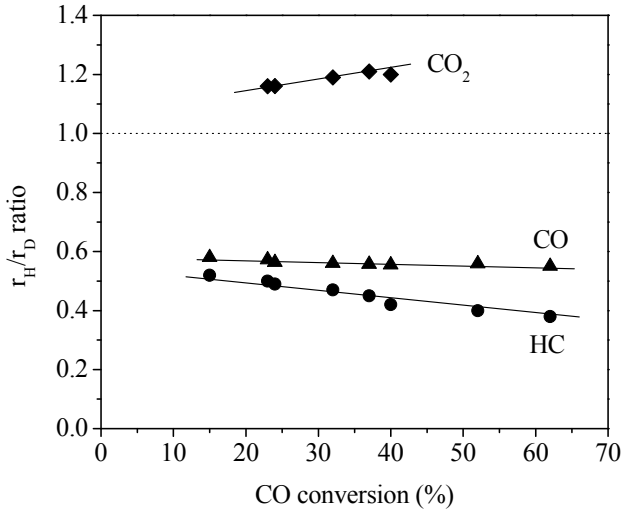

Figure 3.13. r_H/r_D ratio for CO conversion, hydrocarbon and CO_2 formation as a function of CO conversion for H_2/CO or D_2/CO reactants (Zn/Fe=0.1, K/Fe=0.02, Cu/Fe=0.01) at 508 K and 2.14 MPa.

Table 3.2 shows a summary of the consequences of using D_2/CO instead of H_2/CO over the hydrocarbons, water and primary carbon dioxide formation rates. The use of D_2 instead of H_2 increased hydrocarbons formation rate only through the H-assisted CO dissociation mechanism, as indicated by the measured KIE values for the water formation rate. On the contrary, the unassisted pathway is not affected by D_2, which is concluded by the fact that primary carbon dioxide formation rate does not depend on the use of H_2/CO or D_2/CO.

Table 3.2. Summary of the KIE with a Fe-Zn-Cu-K catalyst (Zn/Fe=0.1, K/Fe=0.02, Cu/Fe=0.01) at 508 K and 2.14 MPa.

	r_H (H_2/CO)	r_D (D_2/CO)	KIE
Hydrocarbons (mol h^{-1} g-at Fe^{-1})	3.70	6.50	0.57
Water (mol h^{-1} g-at Fe^{-1})	3.26	6.02	0.54
CO_2 (mol h^{-1} g-at Fe^{-1})	0.44	0.48	0.92
$\rho = r_{HC}^{assisted} / r_{HC}^{unassisted}$	7.4	12.5	-

II. FISCHER-TROPSCH SYNTHESIS ON COBALT CATALYSTS

4. Metal colloids as catalysts for the Fischer-Tropsch synthesis.

In this section, we describe our efforts to develop synthetic protocols for Co-based metallic catalysts by using the precipitation of Co and CoO_x species and their subsequent impregnation onto supports modified to prevent significant interaction of oxide precursors with their surfaces. The objectives are to advance our understanding of the processes involved in deposition and stabilizing Co metal clusters and to use this knowledge to prepare catalysts with higher dispersion and oxidative and sintering stability.

4.1. Experimental methods.

4.1. Catalyst preparation.

ZrO_2/SiO_2 supports with 3.2Zr nm^{-2} were prepared by impregnation of SiO_2 (Davison Grace 62, 287 m^2g^{-1}, treated in dry air at 873 K for 16 h before use) with an aqueous zirconyl nitrate (Aldrich, 99.99 %) in deionized and doubly-distilled water (DDI), and the impregnation was carried out at 373 K in air. The supports were treated in flowing dry air (Praxair, extra dry) by increasing the temperature from ambient to 773 K at 0.17 K s^{-1} and holding at this temperature for 3 h.

ZrO_2/SiO_2 was also prepared via homogeneous deposition-precipitation. 6 g of SiO_2 (Davison Grace 62, 287 m^2 g^{-1}, treated in dry air at 873 K for 16 h before use), 2.8 g of zirconyl nitrate (Aldrich, 99.99 %) and 1 g of urea (ACROS, 99 %) were added into 50 cm^3 of deionized and doubly-distilled water DDI under vigorous stirring at ambient temperature. The suspension was stirred at 363 K for 5 h. After evaporation of water at 373 K, the samples were treated in flowing dry air (Praxair, extra dry) by increasing the temperature from ambient to 773 K at 0.17 K s^{-1} and holding this temperature for 3 h.

ZrO_2/SiO_2 was also prepared by using zirconium (IV) ethoxide. First, 10 g of SiO_2 (Davison Grace 62, 287 m^2 g^{-1}, treated in dry air at 873 K for 16 h before use) was dried in ambient air at 398 K for 6 h. 4 g of zirconium (IV) ethoxide (Alfa Aesar, 99 %), 2 cm^3 of acetic acid (Fischer, 99.8%) and 10 g of pre-treated SiO_2 were added into 140 cm^3 ethanol (Aldrich, 99.5%) at ambient temperature in a dry box. The resulting suspension was stirred at ambient temperature for 12 h. After filtering and washing with ethanol solution, the samples were treated in flowing dry air *(Praxair, extra dry)* by increasing the temperature from ambient to 953 K at 0.17 K s^{-1} and holding at this temperature for 3 h [31].

a) Preparation of Co supported catalysts via incipient wetness impregnation: A Co/SiO_2 (11 wt.%) was prepared by incipient wetness impregnation of SiO_2 (Davison Grace 62, 287 m^2g^{-1}, treated in dry air at 873 K for 16 h before use) with $Co(NO_3)_2{\cdot}6H_2O$ (Aldrich, 99.999%) in DDI water. Impregnation was carried out in air at 373 K. The catalyst was treated in flowing dry air (Praxair, extra dry, 1.67 cm^3 s^{-1}) by increasing the temperature from ambient to 673 K at 0.17 K s^{-1} and holding it there for 4 h.

The $Co/ZrO_2/SiO_2$ catalysts with different Co loading (11 wt.%, 20 wt.%) were prepared by incipient wetness impregnation of ZrO_2/SiO_2 (3.2Zr nm^{-2}) with $Co(NO_3)_2{\cdot}6H_2O$ (Aldrich, 99.999 %) in DDI water. Impregnation was carried out in air at 373 K. The catalysts were treated in flowing dry air (Praxair, extra dry, 1.67 cm^3 s^{-1}) by increasing the temperature from ambient to 673 K at 0.17 K s^{-1} and holding there for 4 h.

b) Preparation of Co supported catalysts via homogeneous deposition-precipitation: 0.72 g of urea (ACROS, 99 %) and 1.2 g of $Co(NO_3)_2{\cdot}6H_2O$ (Aldrich, 99.999 %) were added into 65

cm^3 of DDI water. After addition of 2 g of the ZrO_2/SiO_2 support (3.2 Zr nm^{-2}), the temperature of solution was increased to 363 K and held for 12 h. The resulting pink suspension was subsequently cooled down to ambient temperature and filtered. The resulting solid was dried at 373 K in air and treated in flowing dry air (Praxair, extra dry) by increasing the temperature from ambient to 673 K at 0.17 K s^{-1} and holding it there for 4 h.

*c) Preparation of Co supported catalysts via inverse micelles: F*irst, a toluene and DDI-water mixture was bubbled with Ar (Praxair, 99.9 %) for 2 h to remove the oxygen. 15 g of didodecyldimethylammonium bromide (DDAB, Aldrich, >98%) was dissolved in 104 cm^3 of toluene (Aldrich, 99.8 %) to form a 0.3 mol L^{-1} micelle solution. $CoCl_2$ (0.13 g, Aldrich, 99.9 %) was then added to above solution and sonicated to obtain a blue solution. $NaBH_4$ (1.13 g, Aldrich, 99.99 %) was then added in 30 cm^3 of DDI water to produce a 1 mol L^{-1} solution using a separate baker. The 1 mol L^{-1} $NaBH_4$ solution was slowly added to already prepared micelle solution stirring vigorously to reduce $CoCl_2$. A black colloid appears when the reaction is completed [32]. Subsequently, 0.5 g of SiO_2 was added to the colloidal solution and stirred for 3 h. Acetone solution (Aldrich, 99 %) was used to induce flocculation and then filtered. After using acetone and DDI water to remove the surfactant, the resulting solids were treated in flowing dry helium (Praxair, extra dry) by increasing the temperature from ambient to 573 K at 0.17 K s^{-1} and holding at this temperature for 3 h.

4.1.2. Catalyst characterization.

Powder X-ray diffraction (XRD) measurements were carried out with a Siemens D5000 diffractometer using a CuK_α radiation. The XRD patterns were recorded between $20^o < 2\theta < 70^o$ by step-scanning at 0.05º increments.

Temperature-programmed reduction (TPR) experiments were performed in a flow unit equipped with a thermal conductivity detector (QS-10, Quantachrome Corp.). The sample was placed inside a U-type quartz reactor and treated in 20% H_2 (Praxair, 20 vol.% H_2, 80 vol.% Ar, 1.33 cm^3 s^{-1}) by heating to 1123 K at 0.17 K s^{-1}. The H_2 concentrations were calibrated by reducing pure CuO samples.

Infrared spectra (IR) were recorded with a Mattson RS-1000 Spectrometer in the diffuse reflectance mode with a resolution of 4 cm^{-1}. Samples were ground into fine powders, placed inside a cell positioned within a Praying Mantis mirror assembly (Harrick), and purged with pure He (Praxair, 99.999 %) before heating to 673 K at 0.17 K s^{-1}. All spectra were recorded at ambient temperature.

Chemisorption data were collected with a Quantachrome 1C Autosorb apparatus. The samples were reduced in pure hydrogen (Praxair, 99.999 %) at 673 K for 1 h and then evacuated at this temperature for 10 min to remove chemisorbed hydrogen from the surface. The hydrogen chemisorption was carried out at 373 K (Quantasorb chemisorption analyzer). Adsorption isotherms were extrapolated to zero pressure to obtain the chemisorption uptakes. The dispersion values were calculated from hydrogen uptake and cobalt content assuming a 1:1 stoichiometry of H to surface cobalt atoms. The crystal diameter was calculated by assuming hemispherical crystallites (d (nm) = 0.96/D; D=fractional dispersion) with random surface orientations exposing low-index crystal planes.

4.1.3. Fischer–Tropsch synthesis.

Fischer–Tropsch Synthesis (FTS) rates and selectivities were measured by using a fixed-bed single-pass flow reactor with plug-flow hydrodynamics. The temperature of the catalyst bed was measured by a *K*-type thermocouple (Omega, 0.05-cm diameter, 46-cm length) located within a center thermowell. The flow rates of H_2 [Praxair, 99.999%] and synthesis gas (Praxair, 62 vol. % H_2, 31 vol.% CO and 7 vol.% N_2 internal standard) were controlled by

mass flow controllers (Porter Inc.). Catalysts (105-177 μm) were diluted with SiO_2 (Davison Grace, 62, 105-177 μm) at a mass ratio of 1:2.5 to avoid bed temperature gradients. Before the reaction, the catalyst was reduced in pure H_2 (Praxair, 99.999 %, 2.14 cm^3 (g-catalyst· s)$^{-1}$) within the reactor by heating to 673 K at 0.17 K s^{-1} and holding for 5 h. FTS reactions were carried out at 473 K using 2.15 MPa of synthesis gas (Praxair, 62 vol.% H_2, 31 vol.% CO and 7 vol.% N_2 internal standard). Reactant and product streams were analyzed by an on-line gas chromatograph (Agilent, 6890N) equipped with a cross-linked methyl silicone capillary column (HP-1) and a Porapak Q packed column, respectively [33].

4.2. Effect of ZrO_2 modification on SiO_2 surface silanol groups

Loading a layer of ZrO_2 on SiO_2 surface provides a simple but effective approach to terminate the hydroxyl groups on SiO_2, an approach that may weaken the oxide-support interaction that inhibit reduction of supported metals oxides, CoO_x in the case of this study [34]. In this report, Zr surface densities are reported as the number of Zr atoms per BET surface area (Zr nm^{-2}). Figure 4.1 shows the IR spectra of SiO_2 and ZrO_2/SiO_2 samples treated in flowing helium at 673 K to remove physisorbed water. The SiO_2 spectrum is dominated by an intense sharp band at 3735 cm^{-1}, characteristic of isolated non-interacting surface silanol groups [35,36]. After ZrO_2 deposition, each ZrO_2/SiO_2 sample exhibited the same isolated silanol band in the IR spectra but with lower intensity relative to pure silica. Also the intensities of silanol groups decreased with increasing Zr density on ZrO_2/SiO_2 surfaces (Table 1). Figure 4.2 shows that the Raman spectra of ZrO_2/SiO_2 samples contains a sharp band at 477 cm^{-1}, attributed to three-dimensional amorphous zirconia [37-40]. These results show that these impregnation methods can terminate some of the hydroxyl groups on the SiO_2 surface and that they give a high dispersion of ZrO_2 for samples up to 20 wt.% ZrO_2 loading, for which ZrO_2 crystallites are not detected in their Raman spectra.

Table 4.1. Si-OH intensities of various ZrO_2/SiO_2 samples

Sample	Preparation method	Si-OH intensity
SiO_2	/	1.03
ZrO_2/SiO_2 (0.8 Zr nm^{-2})	Impregnation of zirconium(IV) oxynitrate	0.91
ZrO_2/SiO_2 (3.2 Zr nm^{-2})	Impregnation of zirconium(IV) oxynitrate	0.68
ZrO_2/SiO_2	Zirconium (IV) ethoxide titrate	1.20
ZrO_2/SiO_2 (3.2 Zr nm^{-2})	Homogeneous deposition-precipitation	0.48

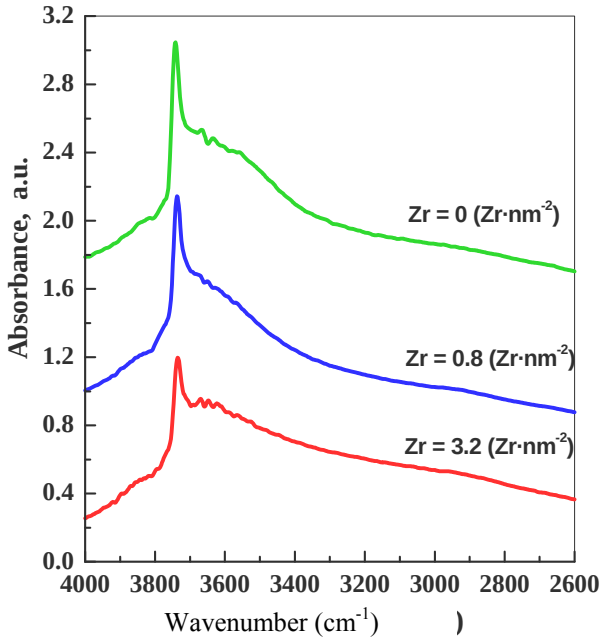

Figure 4.1. IR spectra of SiO_2 and ZrO_2/SiO_2 samples

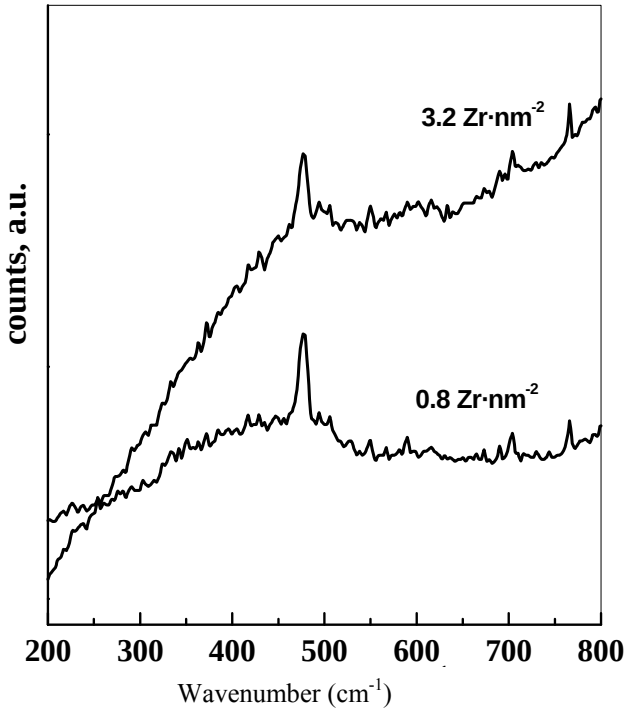

Figure 4.2. Raman spectra of ZrO_2/SiO_2 samples.

In addition to the impregnation method, surface titration (using zirconium (IV) ethoxide reacting with Si-OH on the SiO_2 in ethanol) and homogeneous deposition-precipitation methods were also used to terminate silanol groups, respectively. Although the intensities of hydroxyl groups on ZrO_2/SiO_2 prepared by the homogeneous deposition-precipitation process are weaker than in ZrO_2/SiO_2 prepared by impregnation (Table 4.1), some hydroxyl groups still exist on the surface. These data indicate that the hydroxyl groups on the SiO_2 surface are

difficult to be fully titrated by ZrO_2 modification, perhaps because of steric factors or because of the difficulty in anchoring Zr precursors irreversibly on isolated silanol OH groups.

4.3. Effect of preparation method on cobalt supported catalysts

Monometallic cobalt supported catalysts were prepared by incipient wetness impregnation methods on SiO_2 and ZrO_2/SiO_2 supports. The reduction dynamics of CoO_x/SiO_2 and $CoO_x/ZrO_2/SiO_2$precursors were examined by H_2 temperature-programmed reduction (H_2-TPR). Figure 4.3 shows their H_2-TPR profiles. There are two main H_2 consumption peaks, one at 500-600 K and the other at 600-700 K. Previous studies [41] have shown that Co_3O_4 reduces to Co metal in two steps (Equations 4.1 and 4.2), leading to distinct peaks in the TPR profile. Therefore, the reduction peaks within 500-600 K can be attributed to reduction of Co_3O_4 to CoO, and the CoO formed is then reduced subsequently to Co metal at higher temperatures resulting in broader peaks in the TPR profiles (Fig. 4.3). We also see that $CoO_x/ZrO_2/SiO_2$ samples exhibit similar reduction behavior as CoO_x/SiO_2. Also, the calculated H_2/Co ratios are close to the theoretical values (H_2/Co=1.33), indicating that most of the CoO_x species in these samples can be reduced to cobalt metal within a temperature range of 400-700 K.

$$Co_3O_4 + H_2 \rightarrow 3CoO + H_2O \quad (4.1)$$
$$CoO + H_2 \rightarrow Co + H_2O \quad (4.2)$$

Table 4.2 shows H_2-chemisorption data for supported cobalt catalysts. We see that the application of ZrO_2/SiO_2 as a support improves the Co cluster dispersion leading to smaller Co cluster sizes than for Co/SiO_2. The above H_2-TPR and H_2-chemisorption results suggest that there is no strong interaction between the SiO_2 support and the CoO_x if the CoO_x sizes are large (>20nm), because almost CoO_x species can be reduced at low temperatures (<700 K). ZrO_2 modification has only a weak influence on CoO_x reduction rates but leads to an improvement in Co dispersion.

Table 4.2. H_2 chemisorption results of cobalt supported catalysts

Sample	Co dispersion (%)	Average Co size (nm)
11 wt.% Co/SiO_2	3.1	31
11 wt.% $Co/ZrO_2/SiO_2$ 3.2 (Zr nm^{-2})	4.3	22
20 wt.% $Co/ZrO_2/SiO_2$ 3.2 (Zr nm^{-2})	4.8	20

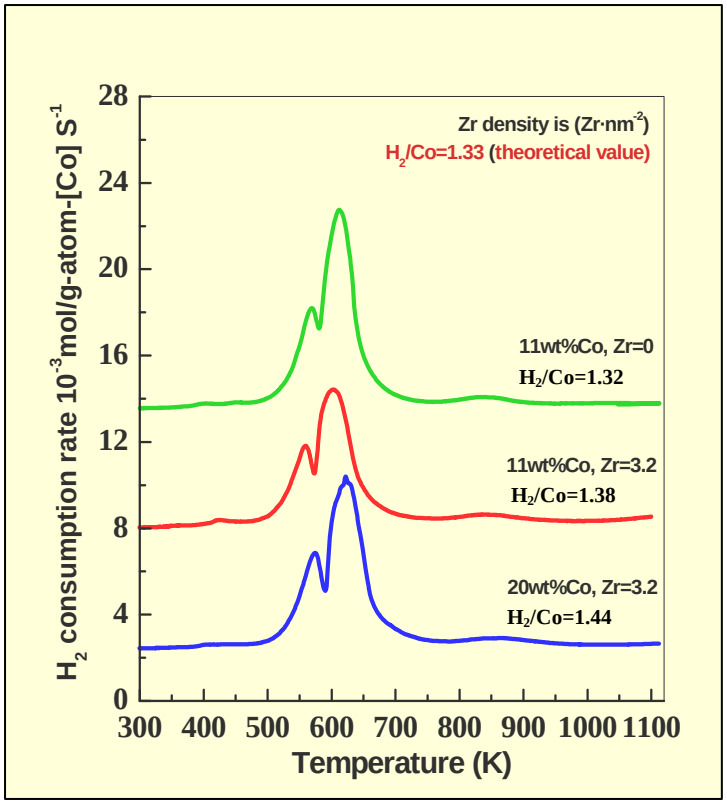

Figure 4.3. H_2-TPR profiles of CoO_x supported SiO_2 and ZrO_2/SiO_2 precursors prepared by incipient wetness impregnation method

Colloidal nanoparticles of transition metals are attractive as precursors to synthesize monometallic or bimetallic supported catalysts, because they can be used to control the metal cluster structure, size, shape, and dispersion, which significantly influence catalyst productivity and selectivity [42,43]. Moreover, the direct synthesis of small metal clusters, instead of metal oxide clusters, on a support using colloidal methods avoids high temperature H_2 reduction processes that often cause sintering of metal clusters. It therefore provides an opportunity to study the catalytic performance of small cobalt clusters in FTS reactions.

In the present study, we have successfully synthesized stable metallic cobalt particles via inverse micelle methods and deposited them onto SiO_2 and modified SiO_2 supports. Figure 4.4 shows TEM micrographs of the resulting Co/SiO_2 catalyst. In the TEM image, small particles with narrow size distributions (3-5 nm) are seen as black spots on the SiO_2 surface, and the high resolution TEM micrographs also show that the individual particles (labeled as white circle in Fig. 4.4b) have lattice fringes consistent with crystalline clusters. X-ray diffraction patterns confirmed the cluster size and crystallinity conclusions reached from these micrographs. As seen in Figure 4.5, the XRD pattern for the Co/SiO_2 catalyst shows a weak and broad diffraction line at ~45°, characteristic of cobalt metal [44]. According to the Scherrer equation, the Co cluster size given by this diffraction line is ~5 nm in excellent agreement with TEM results.

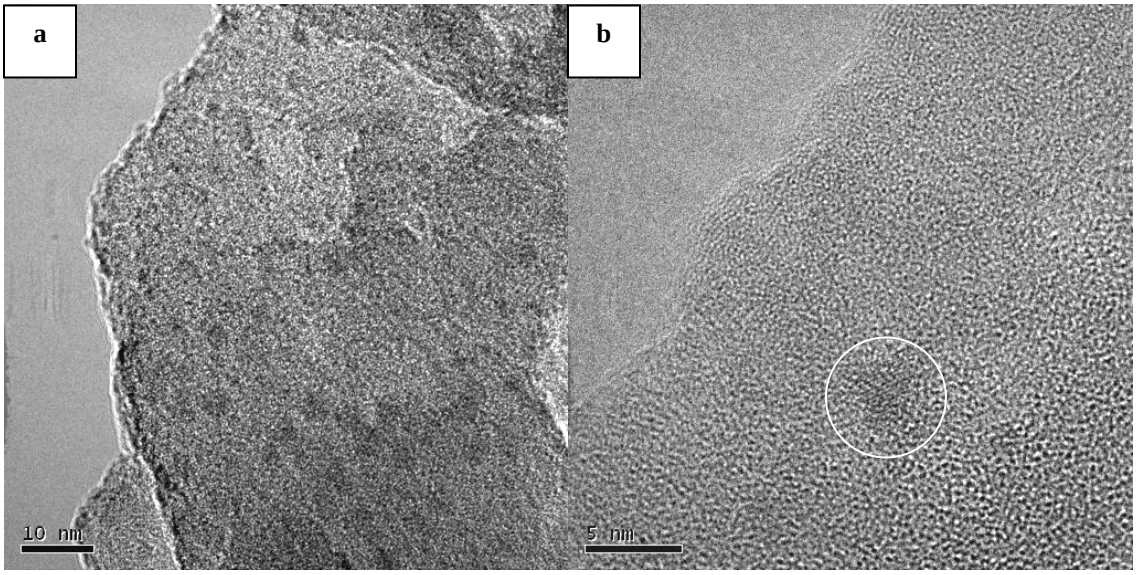

Figure 4.4. TEM photos of Co/SiO_2 prepared by inverse micelle method.

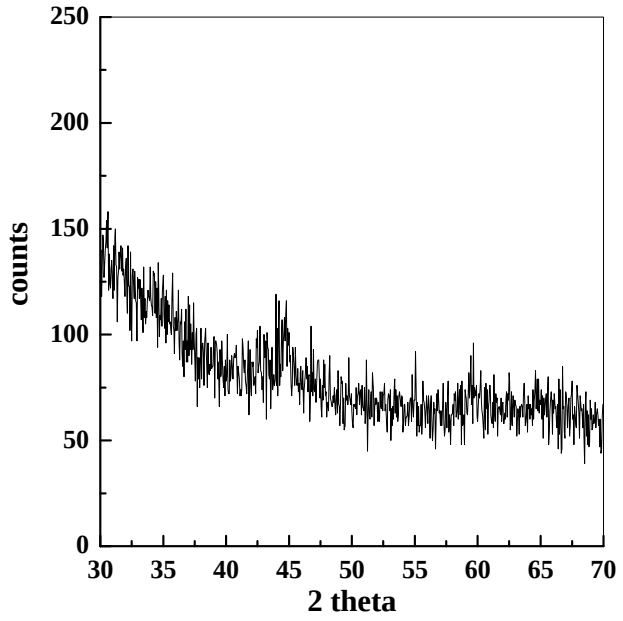

Figure 4.5. XRD pattern of Co/SiO_2 prepared by inverse micelle method.

The H_2-TPR profile in Figure 4.6, however, shows a broad reduction peak at the high temperature ranges (720-1100 K) and the calculated H_2/Co ratio for this peak is smaller than the value expected for Co_3O_4 reduction to Co metal (1.33). These data suggest that small CoO_x and Co metal clusters co-exist on the SiO_2 support. In fact, $NaBH_4$ had already reduced the $CoCl_2$ to metallic Co clusters in the solution, and these Co clusters did not consume H_2 after loading on SiO_2 surface. However, the surfactant removal step (acetone washing) can re-oxidize the metallic Co clusters to CoO_x, because acetone can passivate the small metal particles at ambient temperatures. Once formed, these small CoO_x species strongly interact with SiO_2, requiring high temperatures to become again metallic (Fig. 4.6). These results indicate that the surfactant removal process and the prevention of the re-oxidation of small

metallic Co clusters during this process are essential to form small supported Co metal clusters via colloidal methods.

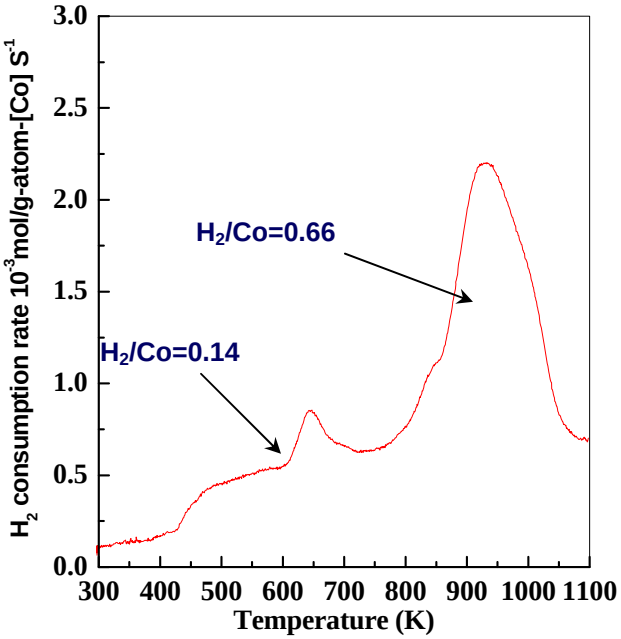

Figure 4.6. H_2-TPR profile of Co/SiO_2 sample prepared by inverse micelle method.

Homogeneous deposition-precipitation (HDP) techniques provide another approach to synthesize high loadings of dispersed metal oxide clusters on supports [45,46]. This method allows the deposition of a soluble metal salt exclusively onto a support surface via gradual and homogeneous introduction of a precipitation agent, for example, hydroxyl ions, to prevent the nucleation of the precursor away from surfaces in the homogeneous phase. The decomposition of urea at 363 K was used to achieve the required slow and homogeneous increase in the pH of a suspension of SiO_2 in a solution of Co nitrate. This method avoids the use of a surfactant. To weaken the interaction between the small CoO_x and support, ZrO_2/SiO_2 was used as support instead of SiO_2. Figure 7 shows the H_2-TPR characterization results for the $CoO_x/ZrO_2/SiO_2$ sample derived from the HDP method. It shows two reduction peaks at relatively low temperatures (375-650 K) but also gives some reduction peaks at temperatures above 800 K, which appear to reflect strong interactions between small CoO_x species and the support. Hence the modification of SiO_2 surfaces by ZrO_2 cannot prevent the formation of some strongly interacting CoO_x species on SiO_2 when CoO_x particles are small, because of residual OH groups on SiO_2 surfaces (Fig. 4.1, Table 4.1).

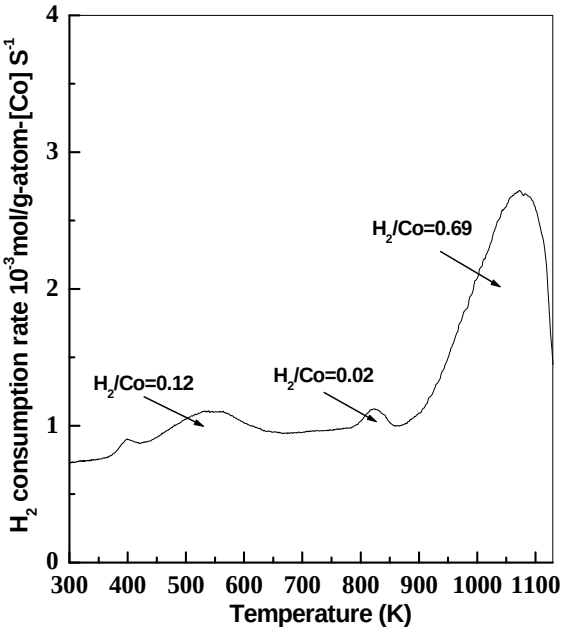

Figure 4.7. H_2-TPR profile of $CoO_x/ZrO_2/SiO_2$ (11 wt.% Co, 3.2 Zr nm^{-2}) sample prepared via homogeneous deposition-precipitation

Table 4.3 shows FTS results for monometallic supported Co catalysts. The Co-time yield is defined as the mole of CO converted per unit time per g-atom Co and Co site-time yield is defined as the mole of CO converted per unit time per surface Co atom (measured by H_2 chemisorption) [41]. Since most of the CoO_x (>90%) cannot be reduced at low temperatures (<673 K) on catalysts prepared by inverse micelle or homogeneous deposition-precipitation methods, these catalysts are not included in Table 4.3.

The use of ZrO_2/SiO_2 as a support improves FTS rates (Co site-time yield and Co-time yield) and C_{5+} selectivity (from 76 to 86 %) while decreasing CH_4 selectivity by a factor of ~2 at the same Co content (Table 4.3). These data suggest that the modification of ZrO_2 on SiO_2 surface not only improves the Co clusters dispersion leading to more accessible sites, but also favors the formation of larger hydrocarbon molecules.

Table 4.3. FTS reaction results of monometallic Co supported catalysts

Catalyst	Co (wt %)	Zr density ($Zr \cdot nm^{-2}$)	Co size (nm)	Co-time yield (mol h^{-1}g-at Co^{-1})	Co site-time yield (mol h^{-1}g-at Co^{-1})	CH_4 selectivity (%)	C_{5+} selectivity (%)
Co/SiO_2	11	0	31	2.4	77.4	12.8	75.9
$Co/ZrO_2/SiO_2$	11	3.2	22	3.5	81.4	6.5	86.5

CO conversion is 17-28%

III. REFERENCES.

1. S. Li, S. Krishnamoorthy, A. Li, G. D. Meitzner, E. Iglesia, J. Catal. 206 (2002) 202.

2. S. Li, A. Li, S. Krishnamoorthy, E. Iglesia, Catal. Lett. 77 (2001) 197.

3. S. Soled, E. Iglesia, S. Miseo, B.A. DeRites, R.A. Fiato, Topics Catal. 2 (1995)193

4. S.A. Eliason, C.H. Bartholomew, Appl. Catal. A: Gen. 186 (1999) 229.

5. M. Luo, R. O'Brien, B.H. Davis, Catal. Lett. 98 (2004) 17.

6. G.P. van der Laan, A.A.C.M Beenackers, Catal. Rev. Sci. Eng. 41 (1999) 255.

7. S. Krishnamoorthy, A. Li, E. Iglesia, Catal. Lett 80 (2002) 77.

8. J. Xu, C.H. Bartholomew, J. Sudweeks, D.L. Eggett, Topics Catal. 26 (2003)55.9. D.B. Bukur, X. Lang, D. Mukesh, W.H. Zimmerman, M.P. Rosynek, C. Li, Ind. Eng. Chem. Res. 29 (1990) 1588.

10. A.P. Raje, R. O' Brien, B.H. Davis, J. Catal. 180 (1998) 36.

11. B. Wu, L. Bai, Z. Zhang, H. Xiang, Y.W. Li, Fuel 83 (2004) 205.12. D.B. Bukur, S.A. Patel, X. Lang, Appl. Catal. 61 (1990) 329.13. S. Li, G.D. Meitzner, E. Iglesia, J. Phys. Chem. B 105 (2001) 5743.

14. C.S. Kuivila, P.C. Stair, J.B. Butt, J. Catal. 118 (1989) 299.

15. J.P. Reymond, P. Meriaudeau, S.J. Teichner, J. Catal 75 (1982) 39.

16. J.F. Shultz, W.K. Hall, T.A. Dubs, R.B. Anderson, J. Am. Chem. Soc. 28 (1956) 282.

17. E.S. Lox, G.F. Froment, Ind. Eng. Chem. Res. 32 (1993) 71.

18. A. Raje, B.H. Davis, ACS Petrol. Chem. Div. Preparation 249 (1996).

19. G.A. Huff, Jr., C.N. Satterfield, Ind. Eng. Chem. Process Des. Dev. 23 (1984) 696.

20. I.C. Yates, C.N. Satterfield, Energy Fuels 5 (1991) 168.

21. V. Ponec, W.A. van Barneveld, Ind. Eng. Chem. Prod. Res. Des. 4 (1979) 268.

22. B.H. Davis, Fuel Process. Technol. 71 (2001) 157.

23. A.T. Bell, Catal. Rev. Sci. Eng. 23 (1981) 203.

24. G.H. Graaf, J.G.M. Winkelman, E.J. Stamhuis, A.A.C.M. Beenackers, Chem. Eng. Sci. 43 (1988) 2161.

25. G.P. van der Laan, A.A.C.M. Beenackers, Appl. Catal. 193 (2000) 39.

26. T. Soller, S. Goldwasser, R.A. Beebe, J. Am. Chem. Soc. 58 (1936) 1703.

27. F. de Pauw, J.C. Jungers, Bull. Soc. Chim. Belg. 57 (1948) 618.

28. J. Nicolai, M. Hout, J.C. Jungers, Bull. Soc. Chim. Belg. 55 (1946) 160.

29. J.T. Kummer, P.H. Emmet, J. Phys. Chem. 55 (1951) 337.

30. A. Ozaki, Isotopic studies of heterogeneous catalysis, Academic Press, New York, 1977.

31. A.C.Q.M. Meijers, A.M. de Jong, L.M.P. van Gruijthuijsen, J.W. Niemantsverdriet, Appl. Catal. 70 (1991) 53.
32. X.M. Lin, C.M. Sorensen, K.J. Klabunde, G.C. Hadjipanayis, Langmuir 14 (1998) 7140.
33. S. Li, S. Krishnamoorthy, A. Li, G. D. Meitzner, E. Iglesia, J. Catal. 206 (2002) 202.
34. A. Hoek, M.F.M. Post, J.K. Minderhoud, P.W. Lednor, U.S. Patent 4499209 (Shell Oil Company).
35. B.A. Morrow, A.J. McFarlan, J. Phys. Chem. 96 (1992) 1395.
36. B.A. Morrow, A.J. McFarlan, Langmuir 7 (1991) 1695.
37. X. Gao, J.L.G. Fierro, I.E. Wachs, Langmuir 15 (1999) 3169.
38. H. Arash, M. Ishigame, Phys. Status Solidi A 71 (1982) 313.
39. E. Anastassakis, B. Papanicolaou, I.M. Asher, J. Phys. Chem. Solids 36 (1975) 667.
40. V.G. Keramidas, W.B. White, J. Am. Ceram. Soc. 57 (1974) 22.
41. E. Iglesia, S.L. Soled, R.A. Fiato, G.H. Via, J. Catal. 143 (1993) 345.
42. R. Narayanan, M.A. El-Sayed, J. Catal. 234 (2005) 348.
43. H. Einaga, M. Harada, Langmuir 21 (2005) 2578.
44. G.N. Glavee, K.J. KIabunde, C.M. Sorensen, G.C. Hadjipanayis, Inorg. Chem. 32 (1993) 474.
45. P. Burattin, M. Chen, C. Louis, J. Phys. Chem. B 102 (1998) 2722.
46. P. Burattin, M. Chen, C. Louis, J. Phys. Chem. B 103 (1999) 6171.